Generative Adversarial Networks-Based Ground Motion Model for Crustal Earthquakes in Japan Considering Detailed Site Conditions

Yuma Matsumoto[1,2], Taro Yaoyama[1], Sangwon Lee[1], Takenori Hida[3], and Tatsuya Itoi*[1]

ABSTRACT

We develop a ground-motion model (GMM) for crustal earthquakes in Japan that can directly model the probability distribution of ground motion acceleration time histories based on generative adversarial networks (GANs). The proposed model can generate ground motions conditioned on moment magnitude, rupture distance, and detailed site conditions defined by the average shear-wave velocity in the top 5 m, 10 m, and 20 m (V_{S5}, V_{S10}, V_{S20}) and the depth to shear-wave velocities of 1.0 km/s and 1.4 km/s ($Z_{1.0}$, $Z_{1.4}$). We construct the neural networks based on styleGAN2 and introduce a novel neural network architecture to generate ground motions considering the effect of source, path, and such detailed site conditions. The resulting 5% damped spectral acceleration from the proposed GMM is consistent with empirical GMMs in terms of magnitude and distance scaling. The proposed GMM can also generate ground motions accounting for the shear-wave velocity profiles of surface soil with different magnitudes and distances, and represent characteristic that are not explained solely by V_{S30}.

1. Department of Architecture, Graduate School of Engineering, The University of Tokyo, Tokyo, Japan, https://orcid.org/0000-0002-8929-9453 (YM) https://orcid.org/0000-0001-9589-4630 (TY) https://orcid.org/0009-0001-3083-9953 (SL) https://orcid.org/0000-0003-3522-7101 (TI); 2. Research Fellow of Japan Society for the Promotion of Science, Tokyo, Japan, https://orcid.org/0000-0002-8929-9453 (YM); 3. Major in Urban and Civil Engineering, Graduate School of Science and Engineering, Ibaraki University, Ibaraki, Japan, https://orcid.org/0009-0005-4349-7592 (TH)

*Corresponding author: itoi@g.ecc.u-tokyo.ac.jp

Cite this article as Matsumoto, Y., Yaoyama, T., Lee, S., Hida, T., and Itoi, T. (2022). Generative Adversarial Networks-Based Ground Motion Model for Crustal Earthquakes in Japan Considering Detailed Site Conditions, *Bull. Seismol. Soc. Am.* **XX**, 1–48, doi: 00.0000/0000000000.

KEY POINTS

- A novel deep generative model-based GMM is proposed, targeting strong-motion records in Japan.
- The probability distribution of ground motion and its source, path, and site conditions can be captured.
- V_{S5}, V_{S10}, V_{S20}, $Z_{1.0}$, and $Z_{1.4}$ are used as proxies for site conditions.

Supplemental Material

INTRODUCTION

Ground-motion models (GMMs) are a critical component in probabilistic seismic hazard analysis (PSHA) (Cornell (1971); Baker et al. (2021)), serving as significant inputs for earthquake engineering. The GMM can evaluate the median as well as the variability of ground motions at a specific site, as functions of source characteristics, propagation path effects, and site conditions. In Japan, various empirical GMMs have been constructed for crustal earthquakes, subduction zone earthquakes, or both (e.g., Fukushima and Tanaka (1990); Molas and Yamazaki (1995); Si and Midorikawa (1999); Nishimura and Horike (2003); Kanno et al. (2006); Zhao et al. (2006); Morikawa and Fujiwara (2013); Ghofrani and Atkinson (2014); Zhao et al. (2016); Si et al. (2022)). These GMMs were developed using the abundant strong motion data recorded by networks such as K-NET and KiK-net (National Research Institute for Earth Science and Disaster Resilience, 2019b). Some GMMs have been constructed using a global database, while introducing a region-dependent term. This approach allows for the development of GMMs with the vast amount of data obtained worldwide, while also taking regional characteristics into consideration. For instance, in the Next Generation Attenuation-West2 (NGA-West2) project (Bozorgnia et al., 2014), a dataset for crustal earthquakes was compiled (Ancheta et al., 2014) and GMMs that can be used in Japan were developed (Abrahamson et al. (2014); Boore et al. (2014); Campbell and Bozorgnia (2014); Chiou and Youngs (2014)). For subduction zone earthquakes, in NGA-Subduction (NGA-Sub) program (Bozorgnia et al., 2022), GMMs were developed in the same manners (Abrahamson and Gulerce (2022); Parker et al. (2022); Kuehn et al. (2023)).

The aforementioned GMMs were constructed for peak ground acceleration (PGA), peak ground velocity (PGV), and 5% damped spectral acceleration. Consequently, hazard curves for these ground motion intensity measures are obtained by PSHA. However, in recent years, it has become common to conduct non-linear dynamic response analysis using acceleration time histories of ground motion as input (Vamvatsikos and Cornell, 2002) for detailed risk assessment of structures (Federal Emergency Management Agency (FEMA), 2018). One approach to synthesizing ground motion time histories using GMMs for dynamic response analysis involves the use of stochastic ground motion models (SGMMs) (e.g., Kameda (1994); Rezaeian and Der Kiureghian (2008); Rezaeian and Der Kiureghian (2010)). In the SGMMs, ground motions are described by a non-stationary stochastic model whose parameters are related to the source, path, and site conditions, and uncertainties in the model parameters are accounted for to represent the variability of the ground motions under the given conditions. Another

approach involves the selection and scaling of ground motions (e.g., Naeim et al. (2004); Bommer and Acevedo (2004); Baker and Cornell (2006)). Ground motions are selected from compiled observed record databases to match the target response spectrum under given conditions. Although this method is widely used in earthquake engineering, it does not always ensure a sufficient number of records for a specific source, path, and site conditions.

In this study, we utilize a deep generative model to develop a GMM capable of directly modeling the ground motion time history data. Deep generative models are probabilistic models that employ deep learning techniques. A key concept of a deep generative model is its ability to capture the inherent distribution of the learned data, and to generate new data that follows this learned distribution. In other words, instead of simply replicating the learned data, a generative model can generate a set of new data that is statistically similar to the original by capturing its underlying probability distribution (Wang et al., 2024). It is generally known that deep generative models, which consist of neural networks with many hidden layers, are capable of learning high-dimensional and complex probability distributions (Ruthotto and Haber, 2021). By applying a deep generative model for ground motion time history data, it is expected to be possible to construct probabilistic models for such high-dimensional data, which has been difficult with existing empirical GMMs and SGMMs. In this study, we refer to such a deep generative model-based GMM as a ground motion generative model (GMGM). The GMGM could become one option for the application of GMMs in earthquake engineering, such as in dynamic response analysis.

Several studies have examined the application of deep generative models for ground motions. Esfahani et al. (2021) utilized an autoencoder on the Fourier amplitude spectra (FAS) of ground motions to estimate the minimum number of predictor variables that is required for a GMM. They also used the trained autoencoder to generate FAS for specific magnitudes and distances. Among the studies that applied deep generative models for ground motion time histories, generative adversarial networks (GANs) (Goodfellow et al., 2014) have been widely adopted. Wang et al. (2019) and Li et al. (2020) examined data augmentation by applying GANs to the generation of ground motion time histories, targeting applications in earthquake detection problems. Similarly, Li et al. (2020) and Wang et al. (2021) have conducted studies on data augmentation for ground motions using a technique called conditional GANs (cGAN) (Mirza and Osindero, 2014) that can specify the generated data with some condition labels. Gatti and Clouteau (2020) proposed a method for generating ground motions up to high-frequency components by combining physics-based simulation methods and GANs. Grijalva et al. (2021) applied GANs to the FAS of ground motions obtained in volcanic events. Matinfar et al. (2023) trained GANs on wavelet-transformed ground motions and developed a method to generate ground motions matching a target response spectrum. Matsumoto et al. (2023) trained GANs for ground motion time histories, and demonstrated that the trained GANs model could adequately approximate the distribution of observed record database. Addressing the characteristics of source, path, and site conditions, similar to GMMs, Florez et al. (2022) demonstrated the capability of cGAN in generating ground motion time histories conditioned on magnitude, distance, and the average shear-wave velocity in the top 30 meters (V_{S30}). Following a similar approach, Esfahani et al. (2022) developed a model named TFCGAN, which learns the time-frequency domain amplitudes of ground

motions conditioned on magnitude, distance, and V_{S30}. Additionally, they demonstrated how the time-frequency amplitudes produced by the trained cGAN could be used to retrieve the ground motion time histories using a phase retrieval technique. Shi et al. (2024) employed an extension of GANs, known as the generative adversarial neural operator (Rahman et al., 2022), to construct a model capable of generating ground motion time histories conditioned on magnitude, distance, V_{S30}, and the style of faulting.

Although various approaches were proposed to apply GANs for ground motion data, most studies have typically described propagation path effects using the source distance and site conditions using V_{S30}. However, such modeling is based on the ergodic assumption (Anderson and Brune, 1999), which may lead to an overestimation of variability in ground motions. Recently, studies on non-ergodic GMMs have been actively conducted to eliminate this ergodic assumption (Lavrentiadis et al., 2023), and in Japan, site-specific GMMs (e.g., Akaba et al. (2024)) and non-ergodic GMMs (e.g., Sung et al. (2024)) have also been developed. Although such modeling can reduce variability, achieving this reduction requires an appropriate modeling of source, path, and site effects. In GMGM, it is also important to address the ergodic assumption and to examine appropriate modeling methods. While the fully non-ergodic GMMs take into account all of the source, path, and site effects, we initially focus on the site effects only. A GMGM that accounts for detailed site conditions could have a potential to eliminate parts of the ergodic assumption.

In this study, we propose a GMGM for crustal earthquakes in Japan, considering detailed site conditions and utilizing GANs on ground motion time history data. The proposed GMGM specifies site conditions using five condition labels: the average shear-wave velocities in the top 5 m, 10 m, 20 m (V_{S5}, V_{S10}, V_{S20}), and the depth to the layer with shear-wave velocities of 1.0 km/s and 1.4 km/s ($Z_{1.0}$, $Z_{1.4}$). By combining these five site conditions with the moment magnitude (M_W) and rupture distance (R_{RUP}), the GMGM is trained on ground motion time history data conditioned on a seven-dimensional vector: $[M_W, R_{RUP}, V_{S5}, V_{S10}, V_{S20}, Z_{1.0}, Z_{1.4}]$. We also propose a novel neural network architecture that can generate ground motion time histories with this seven-dimensional vectors. The quality and distribution of the generated ground motions from the trained GMGM are evaluated, and the performance of the GMGM is demonstrated by comparing it with existing empirical GMMs. We also discuss how well the specified site conditions correlate with the generated ground motions.

The structure of this paper is as follows. The TRAINING DATASETS section describes the dataset used for training of the GMGM. The METHODS section outlines the GANs method and the proposed neural network architectures. The results of the proposed GMGM are shown in ANALYSIS RESULTS AND MODEL EVALUATION section, and the CONCLUSION AND DISCUSSION section presents conclusions and future perspectives based on the detailed site conditions-specified training outcomes. The program code we used for deep learning is available in a GitHub repository (the link provided in DATA AND RESOURCES).

TRAINING DATASETS

Data selection and correction

To compile the training dataset, we collected observed records from shallow crustal earthquakes in Japan. The selection criteria for the earthquakes and records are outlined below.

- Crustal earthquakes that occurred in the Eurasian plate between 1997 and 2016.
- Moment magnitude $M_W > 5$.
- Hypocentral depth less than 30 km.
- Inclusion of both mainshocks and aftershocks that meet the above criteria.
- Observed records at the K-NET stations.
- The rupture distance $R_{RUP} \leq 100$ km.
- Use the two horizontal components of ground motions assuming that they are independent.

Moment magnitude M_W was determined using the moment tensor solution from the F-net (Full Range Seismograph Network of Japan) database (National Research Institute for Earth Science and Disaster Resilience, 2024), and the lower threshold of M_W was set to 5.0 referring to the current practices in PSHA in Japan (Fujiwara et al., 2023). Rupture distance R_{RUP} was calculated as the shortest distance from the rupture area to the station. When M_W is enough small, and the earthquake can be considered as a point source, R_{RUP} was calculated as the hypocenter distance. The final training dataset consists of 21,696 records (after pre-processing) from 62 earthquakes. Each record is a horizontal one-component acceleration time history with sampling rate of 100 Hz. Details of the selected earthquakes are further described in Matsumoto et al. (2023). The locations of the earthquake epicenters and stations are shown in Figure 1, and the magnitude-distance distribution is shown in Figure 2.

It is important to note that the number of earthquakes in the compiled dataset is not very large. Although it is possible to increase the number of target earthquakes included in the training dataset by lowering the magnitude threshold, small M_W values might introduce issues such as the magnitude of completeness (Wiemer and Wyss, 2000). Additionally, there is a concern that the proportion of data within the magnitude range of interest in Japan's PSHA would decrease in the overall dataset, which could decrease the efficiency of the training. Although the characteristics of the datasets are different, the final number of ground motion data, 21,696, is not too small compared to one of the datasets used for training the GANs model of Karras et al. (2020). The proposed GMGM should be expanded to include, e.g., subduction-zone earthquakes, and enable training with a larger dataset. However, such an examination is beyond the scope of this study and is left as a topic for future studies.

Parameters for site conditions

The K-NET database provides P-S logging results at one-meter intervals down to a depth of 20 meters from the surface at each station. Although the GMGM could directly utilize this data as site conditions, we chose to represent surface soil conditions with V_{S5}, V_{S10}, and V_{S20} considering practical applications. Therefore, the surface soil is modeled as a three-layer structure in the GMGM. In many existing GMMs, the surface soil conditions are expressed only by V_{S30}. For comparative purposes, we also calculated V_{S30} using the following empirical formula proposed by Kanno et al. (2006):

$$V_{S30} = 1.13 V_{S20} + 19.5 \tag{1}$$

It is important to note that V_{S30} is not used as a model parameter in the GMGM but is only used for comparison. To account for amplification by deep sedimentary layers, Morikawa and Fujiwara (2013) used $Z_{1.4}$ in their GMM. Abrahamson et al. (2014), Boore et al. (2014), and Chiou and Youngs (2014) used $Z_{1.0}$ as the parameter to represent that amplification. Referring to these studies, we use both $Z_{1.0}$ and $Z_{1.4}$ as the site condition parameters of the GMGM. We obtained the values of $Z_{1.0}$ and $Z_{1.4}$ at the each station included in the complied dataset from the deep subsurface structural model V3.2 provided in Japan Seismic Hazard Information Station (J-SHIS) (National Research Institute for Earth Science and Disaster Resilience, 2019a). It should be noted that the values of $Z_{1.0}$ used in the above three GMMs refer to the depth from the ground surface, whereas the values in J-SHIS database represent the depth from the engineering bedrock, thus the condition settings are not strictly same. The engineering bedrock in the J-SHIS database used in this study is generally defined as the top of a layer with a shear-wave velocity of 500–700 m/s (Fujiwara et al., 2012). Furthermore, $Z_{1.0}$ and $Z_{1.4}$ are selected primarily for the purpose of comparison with existing GMMs, and may not necessarily be optimal as the parameters representing the characteristics of ground motions in our dataset. A future task will be to figure out how to appropriately incorporate the characteristics of deep sedimentary layers into the GMGMs. Through these procedures, we derived a seven-dimensional vector $[M_W, R_{RUP}, V_{S5}, V_{S10}, V_{S20}, Z_{1.0}, Z_{1.4}]$ as a condition label for each observed record.

Data pre-processing

In the compiled dataset, each ground motion was aligned with respect to the P-wave arrival time, which was manually determined by visually inspecting the waveform. Oscillations caused by different events, such as aftershocks occurring shortly after the mainshock, were identified and removed based on visual inspection of the waveform. To increase the number of training data, ground motion time histories, which were obtained by rotating the two horizontal components by 45 degrees and separating each component, were added to the dataset. Florez et al. (2022) and Esfahani et al. (2022) used a 40-second-long time window starting from the P-wave onset. However, in this study, we used a time window that is nearly twice as long to ensure that the portions of large amplitude were retained for almost all observed records. The data length of each ground motion was set to 7,992 (79.92 s) by truncating the end of each record. When the length of the original record was

less than 7,992, zeros were appended to the end to equalize the data length across the dataset. This setting ensures that for approximately 95% of the ground motions in the dataset, the time-window includes vibrations that account for at least 99% of the total cumulative power. A cosine taper was applied to the final 100 steps, and 100 zeros were appended to the start and finish of the records in order to lessen edge effects and stabilize the learning process. The sampling frequency was not changed from 100 Hz, and no band-pass filter was applied. Consequently, ground motion acceleration time histories with a duration of 81.92 s (8,192 samples), starting 1.0 second before the onset of the P-wave, were obtained.

Training of GANs models can be unstable (Arjovsky et al., 2017). To improve the stability of the learning process, normalization techniques are commonly employed within the neural network architecture (Radford et al., 2016). Therefore, in this study, the waveforms and their amplitudes are learned separately to improve model performance. Each observed record amplitude was normalized by its PGA, and the PGA value was appended to the corresponding condition label to form an eight-dimensional vector. Then, normalization was also performed on each element of the condition label vectors, ensuring a mean of zero and a standard deviation of 0.1.

METHODS

GANs

GANs consist of two deep neural networks: a generator G and a discriminator D. The generator G receives a noise vector $\mathbf{z} \sim \mathcal{N}(\mathbf{0}, \mathbf{I})$ as input to generate new data $G(\mathbf{z})$ (referred to as generated data). The discriminator D takes both observed data $\mathbf{x}$ and generated data $G(\mathbf{z})$ as input and estimate the probability that the input is observed data. GANs are trained through an iterative process where the generator and the discriminator are alternately updated. The discriminator is trained to correctly distinguish between the observed and generated data, whereas the generator attempts to produce data that the discriminator will mistakenly identify as observed data. When appropriately trained through such procedures, the discriminator is known to accurately capture the distribution of the learned dataset, enabling the generator to generate realistic new data that follows this learned distribution (Ruthotto and Haber, 2021).

Florez et al. (2022) and Esfahani et al. (2022) used a GANs model known as Wasserstein GAN with gradient penalty (WGAN-GP) (Gulrajani et al., 2017) to construct their models. In our previous study (Matsumoto et al., 2023), we also used the WGAN-GP. However, in this study, we propose a model based on styleGAN2 (Karras et al., 2020), which has achieved higher quality data generation, to construct the GMGM. As the preliminary analyses, we trained some different models using the dataset compiled in the TRAINING DATASETS section. The model based on styleGAN2 was superior to the model based on WGAN-GP in terms of the quality of the generated data and the accuracy in approximating the data distribution. A key feature of styleGAN2 is the architecture of its generator. The generator G of styleGAN2 is composed of two neural networks: the mapping network f and the synthesis network g. The mapping network takes the noise vector $\mathbf{z}$ as input and output a vector $\mathbf{w}$, referred to as the intermediate latent variable. The synthesis network then takes this intermediate latent variable as

input and output generated data $g(\mathbf{w})$ (equivalent to $G(\mathbf{z})$). In conventional GANs, the generator learns the correspondence between the noise vector $\mathbf{z}$ that follows a normal distribution and the observed data $\mathbf{x}$. However, observed data $\mathbf{x}$ are typically not distributed according to a normal distribution. By transforming the noise vector $\mathbf{z}$ into an intermediate latent variable $\mathbf{w}$, the input of the synthesis network is not sampled according to any fixed distribution, but its sampling density is induced by a learned mapping $f(\mathbf{z})$. This would make it easier for the synthesis network to learn the relationship between the intermediate latent variables $\mathbf{w}$ and observed data $\mathbf{x}$ (Karras et al., 2021).

Following the method of Karras et al. (2020), we set the objective function for the generator training as follows:

$$\min_{\theta} \mathbb{E}_{\mathbf{z}} \left[\log(1 - D(G(\mathbf{z}; \theta)))\right] + \mathbb{E}_{\mathbf{w},\mathbf{u}\sim\mathcal{N}(0,\mathbf{I})} \left(\left\|\mathbf{J}_{\mathbf{w}}^{\mathrm{T}}\mathbf{u}\right\|_2 - a\right)^2 \tag{2}$$

where θ is the parameters of the generator, $\mathbf{J}_{\mathbf{w}}$ is the Jacobian matrix $\mathbf{J}_{\mathbf{w}} = \partial g(\mathbf{w})/\partial \mathbf{w}$, and a is the constant. The first term is the logistic loss of the normal GANs (Goodfellow et al., 2014), and the second term is the regularization term. Similarly, we set the objective function for the discriminator training as follows:

$$\min_{\psi} -\mathbb{E}_{\mathbf{x}} \left[\log D(\mathbf{x}; \psi)\right] - \mathbb{E}_{\mathbf{z}} \left[\log(1 - D(G(\mathbf{z}); \psi))\right] + \frac{\gamma}{2}\mathbb{E}_{\mathbf{x}} \left[\|\nabla D(\mathbf{x}; \psi)\|^2\right] \tag{3}$$

where ψ is the parameters of the discriminator, and γ is the constant. The first and second terms are the logistic losses of the normal GANs (Goodfellow et al., 2014), and the third term is the regularization term called R_1 regularization (Mescheder et al., 2018).

Proposed neural network architecture of the GMGM

In this section, we introduce the overview of our newly proposed neural network architecture of the GMGM. For more detailed information on the neural network architecture and their parameter settings, please refer to our GitHub repository.

The overall architecture of the GMGM is shown in Figure 3. The generator takes the noise vector as input and generates a ground motion along with a corresponding condition label. The discriminator, receiving pairs of ground motion and condition label as input, outputs the probability that the inputs are observed records. Since the conventional styleGAN2 model cannot handle condition labels, we made several modifications to the network configurations of Karras et al. (2020). An overview of the proposed neural network architecture of the generator is shown in Figure 4 (a). A new label generation network h was added to generate the condition labels using the feature maps in the final layer of the synthesis network as input. The architectures of the mapping network and synthesis network are almost same as the model configuration by Karras et al. (2020), however, the parameters of the neural networks were modified to fit the data shape of the ground motions. The mapping network consists of eight fully connected layers, using leaky ReLU (Maas et al., 2013) as the activation function. Skip connection (Karras et al., 2018) is used to construct the synthesis network, and both ELU (Clevert et al., 2016) and leaky

ReLU are used as the activation function. The label generation network consists of eight fully connected layers, with leaky ReLU employed as the activation function.

An overview of neural network architecture of the discriminator is shown in Figure 4 (b). The discriminator receives the ground motion data and label data in different neural networks. The neural network for the ground motion data was constructed in the same way as the generator, modifying the neural network configurations and parameters of Karras et al. (2020). The residual network (He et al., 2016) is utilized, and leaky ReLU is applied as the activation function. We introduced a three fully connected layers for label data referring to a configuration called projection discriminator (Miyato and Koyama, 2018). The outputs of this introduced network are combined with the feature maps of the network for ground motion data by taking inner product. Through this process, the discriminator is able to comprehend the information from the condition labels in an appropriate manner (Miyato and Koyama, 2018).

In the preliminary numerical experiments, it was observed that altering the hyperparameters proposed by Karras et al. (2020) tended to decrease the model performance. Therefore, most hyperparameters were determined according to Karras et al. (2020). The learning rate was set to 0.002, the batch size was 64, and the dimensions of $\mathbf{z}$ and $\mathbf{w}$ were both set to 512. Adam (Kingma and Ba, 2017) was used as the optimization method. The deep learning and the construction of neural networks were carried out using the Python library PyTorch (Paszke et al., 2019). For other hyperparameter settings, please refer to our GitHub repository.

ANALYSIS RESULTS AND MODEL EVALUATION

The GMGM was trained using the compiled dataset, and the trained model generated 100,000 different ground motions and corresponding condition labels. Several post-processing steps were performed on the each generated ground motion. Initially, the offset was removed so that mean acceleration becomes zero. Then a fourth-order Butterworth filter was applied with 0.1 Hz low-frequency cutoff and 20 Hz high-frequency cutoff. The accelerations in the first and last two seconds were set to zero, similar to the conditions of the training data. Finally, the amplitudes of each generated ground motion were recovered by multiplying the values of PGA in the corresponding generated condition labels. In this section, we evaluate the performance of the GMGM using these 100,000 generated ground motions and condition labels.

Generated ground motion waveforms

We first evaluate the performance of the GMGM by visually checking the generated data. Figures 5 and 6 show the ground motion waveforms of observed records and generated ground motions for different magnitude, distance, and V_{S30} scenarios, respectively. The ground motion waveforms associated with other scenarios are shown in Figures S1–S4 of the supplementary materials. For Figures 6, S2, and S4, we also show the corresponding raw generated ground motion waveforms (without any post-processing) in Figures S5–S7 of the supplementary materials to confirm the impact of post-processing. V_{S30} for each generated ground motion was calculated from the generated V_{S20} using equation 1. The GMGM appropriately captures

waveform characteristics such as the onset of P-waves and S-waves, as well as the envelope shapes. The amplitude scaling with magnitude and distance is generally well represented, and the relationships between distance and duration, as well as between distance and P-S time, are also appropriate. Moreover, focusing on the values of V_{S30}, lower frequency ground motions are generated in conditions of soft soil where $V_{S30} < 300$ m/s, compared to those of stiff soil where $V_{S30} > 300$ m/s. In the data of row 3 and column 2 in Figures 5 and 6, a tendency for subsequent vibrations to have lower frequency components in soft soil condition is also captured. The more detailed examinations of the correspondence between ground motions and site conditions are conducted in Evaluation considering detailed site conditions subsection.

Overall characteristics of generated ground motions

A key characteristic of the GMGM is its ability to directly learn the probability distribution of ground motion time histories. Therefore, we examine the distribution of the generated ground motions by comparing it with that of training dataset. The evaluation is conducted by examining the following five indices used in Rezaeian and Der Kiureghian (2008) and Rezaeian and Der Kiureghian (2010) to represent the characteristic of ground motions:

1. Arias intensity, I_A.
2. Significant/Relative duration of ground motion, D_{5-95}.
3. Significant/Relative duration of ground motion, D_{5-45}.
4. Zero-level crossing rate, ν.
5. Mean of the rates of negative maxima and positive minima, η.

Arias intensity (Arias, 1970) is a measure of total energy contained in the ground motion and is defined as:

$$I_A = \frac{\pi}{2g} \int_0^{t_d} a^2(t) \mathrm{d}t \tag{4}$$

where g is the gravitational acceleration, t_d is the total duration of ground motion, and $a(t)$ is the acceleration at time t. We set $g = 980.665$ cm/s^2. Significant duration (Bommer and Martínez-Pereira, 1999) is widely used as an index for assessing the ground motion duration (Hancock and Bommer, 2006). The value of D_{5-95} is defined as the time interval required for the cumulative power of the ground motion to reach from 5% to 95% of the total cumulative power, and generally corresponds to the duration of strong motion (Trifunac and Brady, 1975). D_{5-45} is also defined as the time interval from 5% to 45%, and corresponds to the time at the middle of the strong-shaking phase (Rezaeian and Der Kiureghian, 2010). The Zero-level crossing rate ν is adopted to characterize the dominant frequency in ground motion (Rezaeian and Der Kiureghian, 2008), and we calculated the value of ν as the mean of zero-level up-crossing rate and zero-level down-crossing rate. Negative maxima and positive minima are used to characterize the bandwidth of ground motions (Rezaeian and Der Kiureghian, 2010). It is known that a ground motion with wider bandwidth tends to have larger η. We defined η as the mean of the rates of negative maxima and positive minima.

We calculated the values of these five indices for both observed records and generated ground motions. Note that the values of ν and η were calculated for the vibrations in the time interval corresponding to D_{5-95}, and observed records are filtered with the same Butterworth filter used for post-processing of generated ground motions. Figure 7 shows the comparison results of cumulative distribution function (CDF) of each index. Although the generated ground motions tend to have a little smaller D_{5-45} values, the distributions of I_A and D_{5-95} are consistent with that of observed records. This means that the GMGM captures the temporal characteristic of observed records with reasonable accuracy. The distribution of ν also shows a good agreement. The distribution of η indicate that ground motions in the tails of the distribution of observed records are not generated extensively, however, the overall distribution of generated ground motions is generally matched with that of observed records. The GMGM captures the overall characteristics of the observed records in terms of both temporal and frequency characteristics, and is an appropriate probabilistic model of ground motion time histories that approximates the distribution of learned dataset.

Overall characteristics of generated condition labels

In our proposed GMGM, both the ground motion data and the corresponding condition labels are generated simultaneously. This subsection compares the distribution of the generated condition labels with that of the training dataset.

First, the correlations among M_W, R_{RUP} and PGA are compared between the observed records and the generated data, as shown in Figures 8 (a), (b), and (c). For all three labels, the distribution of the generated data generally matches that of the observed records, and the correlations between the condition labels are appropriately modeled. Next, we compare the distributions of the site condition labels, as shown in Figures 8 (d), (e), (f), and (g). It should be noted that the values of $Z_{1.0}$ and $Z_{1.4}$ used in this study represent the depth from the engineering bedrock. The distribution of each label of the generated data also generally matches the distribution of the observed records. Regarding the correlations among the labels of surface soil conditions, the trend that deeper layers tend to have higher shear-wave velocities is captured. Regarding the relationship between $Z_{1.0}$ and $Z_{1.4}$, according to the definition of the index, $Z_{1.0} \leq Z_{1.4}$. Figure 8 (g), which compares the relationship between $Z_{1.0}$ and $Z_{1.4}$, shows that the generated data satisfy this relationship. From these results, it can be concluded that the generated condition labels approximate the distribution of the observed records in training dataset.

Examination of the latent space

In our previous study (Matsumoto et al., 2023), we examined the learning state of the GANs model by checking the distribution of the latent space. In this subsection, we investigate the distribution of the latent space $\mathcal{W}$, where the latent variables $\mathbf{w}$ are distributed. Because $\mathcal{W} \subset \mathbb{R}^{512}$ is a high-dimensional space and direct evaluation is difficult, we use UMAP (McInnes et al., 2020), a dimensionality reduction technique, to visualize the latent space by transforming the latent variables into 2D data. UMAP performs non-linear dimensionality reduction based on manifold learning and is widely used for visualization of high-dimensional data.

Targeting the 100,000 generated data points, we performed dimensionality reduction using UMAP on the corresponding latent variables $\mathbf{w}$. The analysis was conducted using the Python library umap-learn, with Euclidean distance as the metric and the hyperparameters set to n_neighbors = 200 and min_dist = 0.4. The distribution of the latent variables $\mathbf{w}$ is shown in Figure 9. As an example, the figure shows results color-coded by Arias intensity calculated from the generated ground motion time histories, as well as the generated moment magnitude and rupture distance values. Other results, color-coded by other ground motion characteristics indices used in the "Overall characteristics of generated ground motion" subsection and condition labels, are available in Figure S8 of the supplementary materials. It is important to note that the UMAP dimensionality reduction was performed solely on the latent variables $\mathbf{w}$, without using any information about the corresponding generated ground motions or condition labels. Figure 9 demonstrates that generated data with similar Arias intensity, moment magnitude, and rupture distance values are located close to each other in latent space. Moreover, the values of Arias intensity are particularly high in the upper left and lower right of the distribution, corresponding to regions with larger moment magnitudes and shorter rupture distances. The relationship between ground motion characteristics and condition labels is generally appropriately even in the latent space, and the GMGM is considered to be well-trained.

Characteristics of near-field ground motions

Near-field ground motions containing strong velocity pulse have caused destructive damage to structures (e.g., Pitarka et al. (1998); Lin et al. (2018)), and are one of the critical ground motions that should be considered in earthquake engineering. Following the numerical integration of the generated ground motions, the Baker (2007) method was applied to classify and extract the velocity pulses. In the numerical integration of the generated data, a fourth-order Butterworth filter (cutoff frequency 0.2Hz) was used to remove the low frequency components to prevent the noise from them. It should be noted that while the method of Baker (2007) was designed to be applied to the fault normal components of ground motions, the generated ground motions by the GMGM do not contain information on the positional relationship with the fault plane. Therefore, it was applied directly to the generated ground motions.

First, following the evaluation in our previous study (Matsumoto et al., 2023), we compare the distribution of following pulse indicator values proposed by Baker (2007):

$$\text{Pulse indicator} = \frac{1}{1 + \exp(-23.3 + 14.6 v_r + 20.5 E_r)} \tag{5}$$

where v_r is the PGV of the residual data, which is obtained by subtracting the extracted pulse from original velocity data, and E_r is the total accumulate power of residual data divided by that of original data. Pulse-like ground motion tends to have high pulse indicator value. Figure 10 shows the CDF of the pulse indicator of observed records and generated ground motions. Although the proportion of pulse-like ground motion in the generated data is slightly smaller than in the observed records dataset, the overall trend of the distribution is generally consistent. Figure 11 shows the examples of the original velocity

waveforms which were classified as pulse-like ground motion and corresponding extracted pulse waveforms. A clear velocity pulse is found in generated ground motion with the near-filed setting. The proposed GMGM is capable of generating ground motions with engineering-significant characteristic.

Statistical evaluation of the FAS

In this subsection, we conduct statistical performance evaluation of the GMGM. Following the evaluation method of Florez et al. (2022) and Esfahani et al. (2022), we compare the distributions of observed and generated FAS with different M_W, R_{RUP}, and V_{S30} scenarios. Figure 12 compares the logarithmic means and logarithmic standard deviations (std) of the FAS of both observed records and generated ground motions. The bins of the condition labels are determined so that enough number of observed records are contained. The generated FAS are generally consistent with observed FAS in frequency range [1, 20] Hz. In comparisons under relatively small M_W conditions, the generated ground motions contain many low frequency components regardless of R_{RUP} or V_{S30}, resulting in an overestimation particularly in the region below 0.5 Hz. On the other hand, in the region with larger magnitudes range $6.7 \leq M_W \leq 6.9$ (Figure 12 (a)), the generated data agree with the observed records in wider frequency range [0.1, 20] Hz. This trend may be attributed to the influence of the generative processes of the GMGM. The constraint that the acceleration returns to zero under normal conditions is not included in the GMGM. As a result, regions with small amplitudes periodically experience slight deviations from the zero line, which could result in low frequency noise. As small magnitude earthquakes do not cause oscillations with low frequency components, the effect of low frequency noise is notably evident in the range of $5.5 \leq M_W \leq 5.7$ (Figure 12 (c)). The frequency bands for which the distribution of the generated FAS agrees with the FAS of observed records are generally comparable to those examined in Florez et al. (2022) and Esfahani et al. (2022).

Comparison with empirical GMMs

The generated results of the GMGM are compared with the prediction of the following two empirical GMMs:

1. Morikawa and Fujiwara (2013) (MF13) GMM
2. Abrahamson et al. (2014) (ASK14) GMM

Morikawa and Fujiwara (2013) proposed two models which differ in amplitude scaling with reference to magnitudes. We utilize a model with a quadratic magnitude term and perform predictions using the following formula:

$$\log_{10} S_a = a\left(M_{W'} - M_{W_1}\right)^2 + bR_{RUP} + c - \log_{10}\left(R_{RUP} + d \cdot 10^{eM_{W'}}\right) + G_d + G_s \tag{6}$$

$$M_{W'} = \min(M_W, M_{W_0}) \tag{7}$$

$$G_z = p_z \log_{10}\left(\frac{\max(Z_{\min}, Z_{1.4})}{Z_0}\right) \tag{8}$$

$$G_s = p_s \log_{10}\left(\frac{\min(V_{S\max}, V_{S30})}{V_0}\right) \tag{9}$$

where S_a is the spectral acceleration value for specific period, a, b, c, d, e, M_{W_0}, M_{W_1}, p_z, p_s, $Z_{\min}$, and $V_{\mathrm{S\,max}}$ are coefficients. G_z is the correction term for amplification by deep sedimentary layers, and G_s is the correction term for amplification by shallow soft soils.

The ASK14 GMM contains some explanatory variables to specify the source conditions. Since the GMGM cannot take into account such detailed source conditions, the following equation is used for the prediction, considering only terms related to site conditions and the region-specific term:

$$\log S_a = f_1(M_W, R_{RUP}) + f_5(\widehat{Sa}_{1180}, V_{\mathrm{S30}}) + f_{10}(Z_{1.0}, V_{\mathrm{S30}}) + Regional(V_{\mathrm{S30}}, R_{RUP}) \tag{10}$$

where $\widehat{Sa}_{1180}$ is the median spectral acceleration on hard rock. For detailed formulation of f_1, f_5, f_{10}, and $Regional(\cdot)$, please refer to Abrahamson et al. (2014).

Distribution. Figure 13 compares the 5% damped spectral acceleration values at periods $T = 0.2$ s and 1.0 s between the generated ground motions and prediction results from the MF13 GMM and ASK14 GMM. The distance scaling of the GMGM is generally consistent with the MF13 GMM, and the variability of the generated data is also in good agreement with the prediction of the MF13 GMM. Compared to the median spectral acceleration values of the ASK14 GMM at $T = 0.2$ s, the values from the GMGM tend to be slightly higher, especially under soft soil conditions. However, the distributions of the spectral acceleration values at $T = 1.0$ s are generally in agreement.

Residual analysis. The median values of the MF13 GMM and ASK14 GMM corresponding to the each generated condition label are predicted, and the residual values ($\log_{10}$[gen/pre], gen is the generated data and pre is the median of the GMMs) are calculated. To align the condition of the dataset, only generate data with $M_W \geq 5.5$ is used for the MF13 GMM predictions. Figure 14 shows the residuals with reference to M_W, R_{RUP}, V_{S30}, and $Z_{1.4}$ compared with the MF13 GMM. The residuals are generally centered around zero regardless of M_W, V_{S30}, and $Z_{1.4}$ values, indicating that the GMGM has appropriately learned the magnitude scaling as well as the amplification characteristics due to shallow soil and deep sedimentary layers. In terms of distance scaling, there is a tendency to slightly overestimate in regions where R_{RUP} is large, and to slightly underestimate in regions with short distances at $T = 1.0$ s. However, across a wide range, the residuals are generally centered around zero, showing that the distance scaling of the GMGM is consistent with reasonable accuracy. Figure 15 shows the residual plots of the GMGM against the ASK14 GMM prediction for each value of M_W, R_{RUP}, V_{S30}, and $Z_{1.0}$. The generated spectral accelerations tend to be slightly larger at $T = 0.2$ s, as also shown in Figure 13. However, the mean values of the residuals remain relatively constant regardless of the values of M_W, R_{RUP}, V_{S30}, and $Z_{1.0}$. The ASK14 GMM includes a term that considers the nonlinear site response based on the values of V_{S30} and $\widehat{Sa}_{1180}$. Our proposed GMGM cas also capture the effect of such

TABLE 1
Values of the condition labels in Figure 16

Condition label	(i)	(ii)	(iii)
M_W	6.4	6.4	6.4
R_{RUP} (km)	34	32	34
V_{S30} (m/s)	409	408	415
$Z_{1.0}$ (m)	4.0	4.0	203
$Z_{1.4}$ (m)	9.0	9.0	217
υ_{0-5} (m/s)	134	238	289
υ_{5-10} (m/s)	512	402	338
υ_{10-20} (m/s)	866	404	400

nonlinearity. These results confirms that the GMGM has adequately learned the scaling of magnitude and distance, as well as of the amplifications by the shallow soil and deep sedimentary layers when compared with the ASK14 GMM.

Evaluation considering detailed site conditions

The performance of the GMGM is assessed in this subsection when site conditions are given in detail by looking at the relationship between generated ground motions and condition labels. First, the shear-wave velocity profile modeled in three layers for the top 20 meters is back-calculated from the generated values of V_{S5}, V_{S10}, and V_{S20} as follows:

$$\begin{aligned} \upsilon_{0-5} &= V_{S5} \\ \upsilon_{5-10} &= \frac{V_{S5}V_{S10}}{2V_{S5} - V_{S10}} \\ \upsilon_{10-20} &= \frac{2\upsilon_{5-10}V_{S5}V_{S20}}{4\upsilon_{5-10}V_{S5} - \upsilon_{5-10}V_{S20} - V_{S5}V_{S20}} \end{aligned} \tag{11}$$

where υ_{0-5}, υ_{5-10}, and υ_{10-20} are the average shear-wave velocity of the first-layer (0-5 m), second-layer (5-10 m), and third-layer (10-20 m) of the surface soil, respectively. Subsequently, generated data with nearly identical values of M_W, R_{RUP}, and V_{S30}, which are used as condition labels of some GMGM (Florez et al. (2022); Esfahani et al. (2022)), are sampled. Figure 16 presents the time-history waveforms, FAS, and corresponding velocity profiles for three generated samples, and Table 1 represents the corresponding condition label values. Note that the FAS was smoothed using a Parzen window with a bandwidth of 0.2 Hz. Even when the values of M_W, R_{RUP}, and V_{S30} are nearly the same, it is evident that the characteristics of the ground motions differ significantly. In Figure 16, the generated ground motion in (i) has large amplitude, and has a peak near 8 Hz in FAS, whereas the generated ground motion in (ii) has relatively smaller amplitude with a peak near 5 Hz in FAS. Examining the corresponding shear-wave velocity profiles, the data for case (i) reveals a velocity profile where the first-layer has a shear-wave velocity of $\upsilon_{0-5} = 134$ m/s, and the second-layer has a shear-wave velocity of $\upsilon_{0-5} = 512$ m/s. This indicates a soft upper layer of 5 meters, underlain by a harder layer beyond 5 meters. Similarly, in case (ii), the top 5 meters also consists of a soft layer, but υ_{0-5} is slightly larger than in (i), and the difference in shear-wave velocities between the first

and second layer is smaller. The high frequency vibrations are amplified due to multiple reflections at the soft surface soil, suggesting that the generated data in (i) shows larger amplitude and higher predominant frequency compared to (ii) due to this amplification.

Furthermore, the data in (iii), while having similar amplitude and shear-wave velocity profile compared to (ii), contain many low frequency components. The $Z_{1.0}$ and $Z_{1.4}$ values for (iii) are relatively high, indicating that the generated ground motions are also consistent with the effect of deep sedimentary layers. The GMGM is capable of representing characteristic of ground motions that cannot be explained solely by V_{S30} value.

Distribution of generated ground motions with specified magnitude, distance, and detailed site conditions

Our proposed GMGM models the joint distribution $p(\mathbf{x}, \mathbf{y})$ of ground motion data $\mathbf{x}$ and corresponding condition labels $\mathbf{y}$, so it cannot directly evaluate the conditional distribution $p(\mathbf{x} \mid \mathbf{y})$. When applying our proposed method to hazard analysis, the distribution $p(\mathbf{x} \mid \mathbf{s}_*)$ under a specific scenario $\mathbf{s}_*$ can be evaluated using rejection sampling (Tavaré et al., 1997) as follows.

1. Using the trained GMGM, generate N data points to obtain the dataset $\mathcal{D} = \{(\mathbf{x}_i, \mathbf{y}_i) \mid i = 1, \cdots, N\}$. Suppose that the joint distribution is represented by this dataset.

$$p(\mathcal{D}, \mathbf{Z}) = \prod_{i=1}^{N} p(\mathbf{x}_i, \mathbf{y}_i \mid \mathbf{z}_i) p(\mathbf{z}_i) \tag{12}$$

   where $p(\mathbf{x}, \mathbf{y} \mid \mathbf{z})$ is modeled by the GMGM, $\mathbf{Z} = \{\mathbf{z}_1, \cdots, \mathbf{z}_N\}$, and $p(\mathbf{z})$ is the prior distribution of the noise vector.
2. Define the scenario to be specified as a random variable $\mathbf{s}$. Here, $\mathbf{s}$ can be defined as $\mathbf{y}$ itself or as a subvector of $\mathbf{y}$.
3. For a given scenario $\mathbf{s}_*$, using some distance metric $d(\cdot, \cdot)$ and a threshold $\epsilon > 0$, the conditional distribution $p(\mathbf{x} \mid \mathbf{s}_*)$ can be evaluated as follows:

$$p(\mathbf{x} \mid \mathbf{s}_*) \simeq \int_{\mathbf{Z}} \int_{\mathbf{Y}} p(\mathbf{x}, \mathbf{y} \mid \mathbf{z}) p(\mathbf{z}) \mathbb{I}(d(\mathbf{s}, \mathbf{s}_*) \leq \epsilon) \mathrm{d}\mathbf{y} \mathrm{d}\mathbf{z} \tag{13}$$

   where $\mathbf{Y} = \{\mathbf{y}_1, \cdots, \mathbf{y}_N\}$ and $\mathbb{I}(\cdot)$ is an indicator function.

In GANs model, for a given input $\mathbf{z}$, a fixed output $\mathbf{x}$, $\mathbf{y}$ is obtained. Thus, the $p(\mathbf{x}, \mathbf{y} \mid \mathbf{z})$ is a delta function, and the probability distribution $p(\mathbf{x}, \mathbf{y})$ is represented by the generated dataset $\mathcal{D}$ through a Monte Carlo representation. Therefore, the integral calculation in equation 13 can be performed as follows:

1. From the generated dataset $\mathcal{D}$, obtain the corresponding $\{\mathbf{s}_i \mid i = 1, \cdots N\}$ for each $\mathbf{y}_i$.
2. For each $\mathbf{s}_i$, accept those that satisfy $d(\mathbf{s}_i, \mathbf{s}_*) \leq \epsilon$ and reject the rest.
3. Retrieve the corresponding $\mathbf{x}_i^*$ from $\mathcal{D}$ for each accepted $\mathbf{s}_i^*$.

The $\mathbf{x}_i^*$ obtained through the above procedure can be regarded as samples following the distribution $p(\mathbf{x} \mid \mathbf{s}_*)$. It is important to note that to evaluate the distribution $p(\mathbf{x} \mid \mathbf{s}_*)$ using this procedure, the number of generated data points N of the dataset $\mathcal{D}$ must be sufficiently large. In this paper, we set $N = 100,000$. This decision was based on the observation that the distributions shown in Figure 7–9 remain relatively unchanged with further data generation, and that a sufficient number of generated samples could be secured through rejection sampling as examined below. Even if other examinations require a larger amount of data, analyses with a larger N can be conducted at a reasonable computational cost, as the computational cost of GANs data generation is low. In this subsection, we examine the distribution of generated ground motions when some different scenarios are specified.

Initially, we consider a simple scenario where $\mathbf{s} = (M_W, R_{RUP}, V_{S30})^{\mathrm{T}}$. Generated data fitting the following criteria were sampled, and 131 data are obtained:

- $5.9 \leq M_W \leq 6.1$
- $25\ \mathrm{km} \leq R_{RUP} \leq 35\ \mathrm{km}$
- $404\ \mathrm{m/s} \leq V_{S30} \leq 426\ \mathrm{m/s}$

We use the Euclidean distance as the metric $d(\cdot, \cdot)$ for each element of $\mathbf{s}$. The values of ϵ were also determined for each element of $\mathbf{s}$. The black dashed line with circles in Figure 17 (a) shows the mean and standard deviation of the acceleration spectra for all 131 sampled generated ground motions. Among the 131 samples, we further extracted two clusters that share similar shear-wave velocity profiles (Cases 1 and 2), i.e., considering $\mathbf{s} = (M_W, R_{RUP}, V_{S30}, \upsilon_{0-5}, \upsilon_{5-10}, \upsilon_{10-20})^{\mathrm{T}}$. The red dashed line with squares (Case 1) and blue dotted line with triangles (Case 2) in Figure 17 (a) shows the mean acceleration spectra of the extracted clusters, and their corresponding shear-wave velocity profiles of each sampled data are shown in Figure 17 (b). Note that the standard deviation of Case 1 and Case 2 are calculated together to ensure a sufficient sample size as follows:

$$\sigma = \sqrt{\frac{(n_1 - 1)\hat{\sigma}_1^2 + (n_2 - 1)\hat{\sigma}_2^2}{n_1 + n_2 - 2}} \tag{14}$$

where n_1 and n_2 are the number of data in Case 1 and 2, respectively, and $\hat{\sigma}_1^2$ and $\hat{\sigma}_2^2$ are the unbiased variance of data in Case 1 and 2, respectively. The mean acceleration spectra varies depending on the soil profile. For example, Case 1 has relatively soft soil condition of top 5 meters, and the spectral acceleration of Case 1 at short period range had larger values. The standard deviations at each period have decreased by specifying the shear-wave velocity profile, and the averaged standard deviation for each period of Case 1 and Case 2 results in about 0.35. According to the study by Morikawa et al. (2008), the standard deviation (total of the within-event and between-events) of the 5% damped spectral acceleration at specific station generally ranges between 0.35 and 0.45. Hikita and Tomozawa (2023) studied the variability of spectral acceleration of single-path ground motions, and the standard deviations approximately ranged between 0.3 and 0.5 in their examination. Although a

strict comparison is challenging due to different settings, the standard deviation obtained in this study is considered to be generally reasonable.

To examine the relationship between the characteristics of generated ground motions and the shear-wave velocity profiles, the amplification spectra at the surface were calculated for Case 1 and Case 2 in Figure 17, considering the third layer (10-20 m) as the reference layer. The analysis was based on the multiple reflection theory, assuming a linear layered structure. Constant Q_s value of 20 was used for damping, and the soil density of each layer was estimated from the shear-wave velocities using the relationships of Gardner et al. (1974). Figure 17 (c) shows the amplification spectra for Case 1 and Case 2, as well as the logarithmic mean of the FAS of the corresponding generated ground motions. The predominant frequencies of the ground motion data match the peaks in the amplification spectra. Additionally, it can be observed that in Case 1, the difference in shear-wave velocity between the first and third layers is greater than in Case 2, exhibiting higher predominant frequency. Compared to Case 2, the FAS of Case 1 has more frequency components around 2 Hz. The values of $Z_{1.0}$ for the generated data in Case 1 are generally between 30 and 60 meters, whereas the values for the generated data in Case 2 are approximately 4.0 meters. This indicates that the frequency characteristics are consistent with the characteristics of the amplification by deep sedimentary layers. It can be concluded that the frequency characteristics of the generated ground motions are generally consistent with the corresponding shear-wave velocity profiles. However, it should be noted that this analysis considers linear site amplification. Given the response spectra values of Cases 1 and 2, it is necessary to consider the nonlinear site response, and this examination focuses on the rough peaks of the spectra.

Data interpolation by GMGM

GANs are known to generate new data samples by interpolating the distribution of a learned dataset (Luzi et al., 2021). In this subsection, we evaluate the data interpolation of the GMGM for generated ground motions and condition labels.

First, Figure 8 (h) compares the distribution of M_W and V_{S30} between the observed records dataset and generated data. While no generated data correspond to the slightly included area of $V_{S30} > 1000$ m/s in the training dataset, new data have been generated within the region where observed records are distributed. For instance, there are no observed records corresponding to $M_W = 6.5$ in the dataset, yet the GMGM also generates data for such regions. Looking at the residual plots in Figure 14, the generated results for $M_W = 6.5$ are consistent with the predictions of the MF13 GMM, indicating the validity of the generated ground motions. The GMGM can generate data for combinations of condition labels that are not included in the observed record database.

Next, we examine the case specifying M_W, R_{RUP}, and the shear-wave velocity profile. We again use the six generated ground motions in Case 2 in Figure 17, which were selected from the 100,000 generated data to have almost identical values of M_W, R_{RUP}, V_{S30}, and shear-wave velocity profile v_{0-5}, v_{5-10}, and v_{10-20}. Table 2 lists the values of M_W, R_{RUP}, and site conditions of the six generated ground motions in Case 2. Although $Z_{1.0}$ and $Z_{1.4}$ were not specified during data selection, these val-

TABLE 2
Values of M_W, R_{RUP}, and site conditions of the six generated ground motions of Case 2 in Figure 17 (generated Data 1 to 6) and site condition values of K-NET station YMG007. The values of the surface soil conditions of the YMG007 station were calculated using the P-S logging data of K-NET database. Since only shear-wave velocity profile up to 10 meters has been obtained at YMG007 station in K-NET database, it is assumed that the shear-wave velocity from 10 meters to 20 meters is identical to the upper layer. Noted that the values of $Z_{1.0}$ and $Z_{1.4}$ represent the depth from the engineering bedrock as discussed in the TRAINING DATASETS section.

-	M_W	R_{RUP} (km)	V_{S30}	υ_{0-5} (m/s)	υ_{5-10} (m/s)	υ_{10-20} (m/s)	$Z_{1.0}$ (m)	$Z_{1.4}$ (m)	**Data type**
Data 1	6.0	29	416	249	377	422	3.9	10	Generated
Data 2	6.0	33	411	246	378	414	4.2	11	Generated
Data 3	6.0	31	418	254	380	420	4.0	10	Generated
Data 4	6.0	32	417	248	387	425	4.0	10	Generated
Data 5	6.0	33	420	249	382	430	3.9	10	Generated
Data 6	6.0	35	416	247	378	424	3.9	10	Generated
YMG007	-	-	418	260	400	400	4.0	10	Observed

ues are also nearly identical across all six ground motions. To investigate the cause of this trend, Table 2 also presents the site conditions of the K-NET station YMG007, whose records were included in the training dataset. The shear-wave velocities, υ_{0-5}, υ_{5-10}, and υ_{10-20}, and the values of $Z_{1.0}$ and $Z_{1.4}$ at the YMG007 station closely align with those of generated Data 1–6, indicating that the generated ground motions are dominated by the characteristics of the observed records at the YMG007 station. This suggests that while the GMGM can interpolate data when only a few condition labels are considered, as shown in Figure 8, such interpolation becomes more challenging as the number of considered condition labels increases. This is because the number of corresponding observed records may become insufficient, leading to the generated data being dominated by specific observed records. This will be discussed further in CONCLUSION AND DISCUSSION section.

Finally, we examine the case where only site conditions were specified. At YMG007 station, two observed records from different earthquakes are obtained in our training dataset. The relationships between these earthquakes and the YMG007 station are shown in Figure 18. Then, generated data having the same site conditions as YMG007 station are sampled, corresponding to the following criteria:

- $225\ \text{m/s} \leq \upsilon_{0-5} \leq 275\ \text{m/s}$
- $355\ \text{m/s} \leq \upsilon_{5-10} \leq 405\ \text{m/s}$
- $395\ \text{m/s} \leq \upsilon_{10-20} \leq 445\ \text{m/s}$
- $3\ \text{m} \leq Z_{1.0} \leq 5\ \text{m}$
- $9\ \text{m} \leq Z_{1.4} \leq 11\ \text{m}$

Figure 19 shows the magnitude-distance distribution of the two observed records at YMG007 station and the sampled generated data. Although no data have been generated for region where R_{RUP} is approximately 100 km, it is evident that data corresponding to combinations of magnitude and distance not included in the observed records have been generated even when specifying detailed site conditions. Therefore, even when the number of considered condition labels is increased, the GMGM is capable of generating data not included in the observed records dataset, provided that the number of condition

TABLE 3
Rupture distance in the earthquake that occurred on March 12, 2011, in northern Nagano Perfecture and site conditions of the target KiK-net staions in Figure 21.

Station	R_{RUP} (km)	V_{S30} (m/s)	$Z_{1.4}$ (m)
TCGH07	77.6	419.5	97.6
NGNH26	70.9	300.5	119.0
NIGH11	25.9	375.0	1651.3

labels used for interpolation remains small. For the data for 42 km $\leq R_{RUP} \leq$ 44 km in Figure 19, time history waveforms and their corresponding acceleration spectra and shear-wave velocity profiles are shown in Figure 20. The frequency characteristics of generated ground motions are generally similar to the observed record, and the magnitude scaling of the amplitude is generally appropriate.

Comparison with the observed records of KiK-net

To examine whether the proposed GMGM appropriately considers detailed site conditions, we compared the generated ground motions with the observed records at KiK-net stations that were not used for the GMGM training. For the target earthquake, we selected the earthquake that occurred on March 12, 2011, in northern Nagano Prefecture. Note that the observed records from the K-NET stations for this earthquake are included in the GMGM training dataset. The moment magnitude was 6.2, and the focal depth was 8.4 km. We selected three KiK-net observation stations: TCGH07, NGNH26, and NIGH11. The epicenter of the earthquake and the locations of the stations are shown in Figure 21, and the rupture distances and site conditions for each station are shown in Table 3.

For each target station, the values of v_{0-5}, v_{5-10}, and v_{10-20} were derived from the P-S logging data of the KiK-net database. From 100,000 generated data, we sampled the data that satisfied the following conditions:

- $6.1 \leq M_W \leq 6.3$.
- Rupture distance within $[R_{RUP} - 5, R_{RUP} + 5]$ for each target station.
- Shear-wave velocity of the i-th layer $v_i (i = 1, 2, 3)$ within $[0.9v_i, 1.1v_i]$ for each target station.

As a result, 13, 30, and 8 generated data samples were selected for the TCGH07, NGNH26, and NIGH11 stations, respectively. The 5% damped response spectra of the observed records and the sampled generated ground motions are compared in Figure 22. Additionally, the median and ± 1 standard deviation interval of the MF13 GMM predictions are also shown. Note that the observed records are shown for the NS and EW components at the ground surface. The shear-wave velocity profiles of the stations and generated data are illustrated at the right panel of the response spectra. For TCGH07 (Figure 22 (a)), although the spectral accelerations of the observed records are slightly smaller in the period range above 0.5 s, the response spectra of the observed records and the generated ground motions generally match. Particularly for components with periods below 0.3 s, the observed records and generated ground motions are in good agreement. In contrast, for NGNH26 (Figure 22 (b)), the

spectral accelerations of the observed records are smaller across a wide period range, showing a tendency for the generated ground motions to be overestimated. The NGNH26 station is located near the Itoigawa–Shizuoka Tectonic Line (ISTL), and the region between the hypocenter and the ISTL has been noted as having a low Q attenuation structure (Nakamura and Uetake (2002); Nakajima and Matsuzawa (2017)). In the proposed GMGM, propagation path effects are modeled solely based on rupture distance. As a result, the GMGM could not adequately evaluate the influence of such propagation path structures. For the NIGH11 station (Figure 22 (c)), the response spectra of the observed records and generated ground motions are in good agreement compared to the analysis results at other stations. This is considered to result from the relatively short rupture distance at the NIGH11 station. The observed record at the NIGH11 station may not be significantly affected by the unmodeled propagation path effects.

In summary, under scenarios that consider detailed site conditions, our proposed GMGM can generally represent the characteristics of observed records at the stations not used for training. However, our GMGM could not appropriately capture the characteristics of the observed records that may be influenced by attenuation structures of the propagation path. To evaluate the characteristics of ground motions at specific sites, it is essential to incorporate such effect in more detail within the GMGM.

CONCLUSION AND DISCUSSION

In this study, we developed a GMM (GMGM) for crustal earthquakes in Japan that can directly generate ground motion time histories with specifying detailed site conditions. The proposed GMGM were developed based on a type of deep generative model, called styleGAN2, and a novel neural network architecture that could serve as a generative model with detailed condition labels were also proposed. The neural network architecture of the GMGM is capable of accounting for site conditions with five values, $[V_{S5}, V_{S10}, V_{S20}, Z_{1.0}, Z_{1.4}]$, in addition to magnitude and distance information. We demonstrated that the characteristics of the generated ground motions are consistent with these condition labels, and ground motions with engineering-significant characteristic can be generated. Furthermore, the amplifications by shallow soil and deep sedimentary layer were shown to be accurately represented, and the GMGM's magnitude and distance scaling were shown to match those of empirical GMMs. Additionally, by modeling the surface soil in three layers, the GMGM could express differences in ground motion characteristics that could not be explained solely by V_{S30}, and generated new data samples with different magnitude-distance settings even when detailed site conditions were specified.

The GMGM constructed in this study does not always produce high-quality ground motions, in some cases, significant noises occur at the end of the waveform. Figure 23 shows an example of such generated result. This type of data tends to be generated, although infrequently, under combinations of condition labels where there are fewer data points in training dataset. The cause of this tendency might be attributed to the influence of the vibrations included in the observed records. Subsequent vibrations believed to be caused by aftershocks were eliminated, as stated in the data preprocessing subsection.

On the other hand, aftershocks left some vibrations that were difficult to pinpoint. Therefore, the observed records in our training dataset might include vibrations like those in the time interval from 40 to 60 s in Figure 23, and it is conceivable that the GMGM has learned such tendencies. The vibrations seen after about 75 s in Figure 23 are not mere noise but resemble a ground motion. This could be due to the characteristics of convolutional neural networks (CNNs). The parts of neural networks of the GMGM have constructed by CNNs, which are known to have a property called equivariance to translation due to parameter sharing (Goodfellow et al., 2016). It is important to improve the performance of the GMGM by carefully examining the data preprocessing procedures and the configuration of the neural networks suitable for generating ground motion data.

GANs generate new data samples by interpolating the distribution of learned dataset. Although interpolation could be performed when a few condition labels are specified, the site conditions specified by the five-dimensional vector $[V_{S5}, V_{S10}, V_{S20}, Z_{1.0}, Z_{1.4}]$ were not well-interpolated. This issue might stem from the *curse of dimensionality*. In the compiled dataset, there are 728 observation stations. The distribution of soil conditions defined by five-dimensional vectors is relatively high-dimensional considering this number of stations. Data points may not be sufficiently dense for effective interpolation when many conditions are specified. This challenge is one of the difficulties in data-driven approaches. As more condition labels are considered in detail for the source, path, and site conditions, the lack of data becomes a more significant issue. Potential solutions to this problem about site conditions include increasing the number of observation stations used in compiled dataset. The performance of the GMGM may be improved by including observed records at KiK-net stations, as they were not used in this investigation. Using simulation-based techniques to estimate ground motion amplifications and predict ground motions at the bedrock using GMGMs could be another way to solve this problem. This approach would require detailed site condition information, and there is a possibility of bias because of the one-dimensional-based modeling (Zhu et al., 2023). However, by combining the GMGM with simulation-based methods, it may be possible to address the issues caused by the lack of data mentioned above in constructing the GMGM.

Previous studies applying GANs to GMM (Florez et al. (2022); Esfahani et al. (2022); Shi et al. (2024)) have constructed models based on cGAN, specifying condition labels for generating ground motions. In contrast, this study generates ground motions and condition labels from normal random inputs without specifying such labels. The advantages and disadvantages of our method compared to cGAN based method are as follows. An advantage is its suitability for generating ground motions when detailed condition labels are specified. As mentioned earlier, GANs approximate the distribution of the learned dataset, making them unsuitable for generating data that would be a complete extrapolation from the dataset range. For example, in the dataset used in this study, the moment magnitudes of the records range from 5.0 to 7.1, making it difficult for the GMGM to generate ground motions for magnitudes like 4 or 8. The distribution of condition labels within the seven-dimensional space is sparse, considering the number of available observed records. Since cGAN requires the specification of condition labels to generate data, such sparsity could make it challenging to appropriately set these labels without exceeding the applicable

range. Consequently, models that specify more detailed condition labels may generate ground motions that ideally should not be generated. Such problems can be avoided by generating condition labels with ground motions at the same time. On the other hand, a disadvantage of our method is the time required to generate ground motions that matches specific condition labels. The frequency of generated data depends on its occurrence in the training dataset, which means data for less common conditions is less likely to be generated. To utilize the GMGM in the filed of earthquake engineering, it is necessary to construct a framework that incorporates rare-event simulation techniques (Bucklew and Bucklew, 2004), which are studied in fields such as structural reliability (Au and Beck, 2001).

Additionally, while this study constructed GMGMs for one horizontal component of ground motions occurred in crustal earthquakes, it is also important from the viewpoint of earthquake engineering to predict ground motions for subduction zone earthquakes and to simultaneously predict three components. Expanding the application range of the GMGM is essential and is a future task. Additionally, our proposed GMGM is a data-driven generative model and cannot be applied to scenarios corresponding to extrapolation areas that are entirely absent from the learned dataset. For predictions that include such areas, utilizing analysis results from physics-based ground motion simulation can be considered. In hazard analysis and engineering applications, it is expected that by using our proposed GMGM and simulation methods according to the scenario, a broader range of problem settings can be addressed. This type of analysis also remains a future task.

DATA AND RESOURCES

The strong motion records and the shear-wave velocity values of the surface soil used in this study can be downloaded through the website of the National Research Institute for Earth Science and Disaster Resilience (NIED; https://www.kyoshin.bosai.go.jp/kyoshin/). The moment magnitude was obtained from the NIED F-net database https://www.fnet.bosai.go.jp/, and the values of $Z_{1.0}$ and $Z_{1.4}$ were obtained from the NIED J-SHIS website https://www.j-shis.bosai.go.jp/. The information regarding the locations of the active segments of the Itoigawa–Shizuoka Tectonic Line was obtained from the Active Fault Database of Japan (https://gbank.gsj.jp/activefault/index_e_gmap.html). The program code used in deep learning is available in the GitHub repository https://github.com/Mat-main-00/ss_gmgm. The list of earthquakes and observation stations used for training is also available on this GitHub repository. The supplementary material is available as a separated document, containing supplemental figures S1–S8, which include the ground motion waveforms generated by the constructed model and the distribution in the latent space.

DECLARATION OF COMPETING INTERESTS

The authors acknowledge that there are no conflicts of interest recorded.

ACKNOWLEDGMENTS

This study was supported by JSPS KAKENHI Grant Numbers JP23H00219 and JP22J23006. The authors extend their gratitude to the Associate Editor Sanjay Singh Bora, Filippo Gatti, and an anonymous reviewer for their review comments and suggestions that enhanced the quality of this study. The authors also extend their thanks to Hiroe Miyake for providing valuable comments on this study.

REFERENCES

Abrahamson, N. A. and Z. Gulerce (2022). Summary of the Abrahamson and Gulerce NGA-Sub ground-motion model for subduction earthquakes. *Earthq. Spectra* **38**(4), 2638–2681.

Abrahamson, N. A., W. J. Silva, and R. Kamai (2014). Summary of the ASK14 ground motion relation for active crustal regions. *Earthq. Spectra* **30**(3), 1025–1055.

Akaba, H., T. Yaoyama, and T. Itoi (2024). Construction of site-specific ground motion model based on multi-output gaussian process. *J. Jpn. Assoc. Earthq. Eng.* **24**(1), 1_73–1_91. (in Japanese with English abstract).

Ancheta, T. D., R. B. Darragh, J. P. Stewart, E. Seyhan, W. J. Silva, B. S.-J. Chiou, K. E. Wooddell, R. W. Graves, A. R. Kottke, D. M. Boore, T. Kishida, and J. L. Donahue (2014). NGA-West2 database. *Earthq. Spectra* **30**(3), 989–1005.

Anderson, J. G. and J. N. Brune (1999). Probabilistic Seismic Hazard Analysis without the Ergodic Assumption. *Seismol. Res. Lett.* **70**(1), 19–28.

Arias, A. (1970). A measure of earthquake intensity. In R. J. Hansen (Ed.), *Seismic Design for Nuclear Power Plants*, pp. 438–483. MIT Press.

Arjovsky, M., S. Chintala, and L. Bottou (2017). Wasserstein generative adversarial networks. In *Proc. of the 34th Int. Conf. on Machine Learning*, pp. 214–223.

Au, S.-K. and J. L. Beck (2001). Estimation of small failure probabilities in high dimensions by subset simulation. *Probabilistic Eng. Mech.* **16**(4), 263–277.

Baker, J., B. Bradley, and P. Stafford (2021). *Seismic Hazard and Risk Analysis*. Cambridge University Press.

Baker, J. W. (2007). Quantitative classification of near-fault ground motions using wavelet analysis. *Bull. Seismol. Soc. Am.* **97**(5), 1486–1501.

Baker, J. W. and C. A. Cornell (2006). Spectral shape, epsilon and record selection. *Earthq. Eng. Struct. Dynam.* **35**(9), 1077–1095.

Bommer, J. J. and A. B. Acevedo (2004). The use of real earthquake accelerograms as input to dynamic analysis. *J. Earthq. Eng.* **8**, 43–91.

Bommer, J. J. and A. Martínez-Pereira (1999). The effective duration of earthquake strong motion. *J. Earthq. Eng.* **3**(2), 127–172.

Boore, D. M., J. P. Stewart, E. Seyhan, and G. M. Atkinson (2014). NGA-West2 equations for predicting PGA, PGV, and 5% damped PSA for shallow crustal earthquakes. *Earthq. Spectra* **30**(3), 1057–1085.

Bozorgnia, Y., N. A. Abrahamson, S. K. Ahdi, T. D. Ancheta, L. A. Atik, R. J. Archuleta, G. M. Atkinson, D. M. Boore, K. W. Campbell, B. S.-J. Chiou, V. Contreras, R. B. Darragh, S. Derakhshan, J. L. Donahue, N. Gregor, Z. Gulerce, I. Idriss, C. Ji, T. Kishida, A. R. Kottke, N. Kuehn, D. Kwak, A. O.-L. Kwok, P. Lin, J. Macedo, S. Mazzoni, S. Midorikawa, S. Muin, G. A. Parker, S. Rezaeian, H. Si, W. J. Silva, J. P. Stewart, M. Walling, K. Wooddell, and R. R. Youngs (2022). NGA-Subduction research program. *Earthq. Spectra* **38**(2), 783–798.

Bozorgnia, Y., N. A. Abrahamson, L. A. Atik, T. D. Ancheta, G. M. Atkinson, J. W. Baker, A. Baltay, D. M. Boore, K. W. Campbell, B. S.-J. Chiou, R. Darragh, S. Day, J. Donahue, R. W. Graves, N. Gregor, T. Hanks, I. M. Idriss, R. Kamai, T. Kishida, A. Kottke, S. A. Mahin, S. Rezaeian, B. Rowshandel, E. Seyhan, S. Shahi, T. Shantz, W. Silva, P. Spudich, J. P. Stewart, J. Watson-Lamprey, K. Wooddell, and R. Youngs (2014). NGA-West2 research project. *Earthq. Spectra* **30**(3), 973–987.

Bucklew, J. A. and J. Bucklew (2004). *Introduction to rare event simulation*, Volume 5. Springer New York.

Campbell, K. W. and Y. Bozorgnia (2014). NGA-West2 ground motion model for the average horizontal components of PGA, PGV, and 5% damped linear acceleration response spectra. *Earthq. Spectra* **30**(3), 1087–1115.

Chiou, B. S.-J. and R. R. Youngs (2014). Update of the Chiou and Youngs NGA model for the average horizontal component of peak ground motion and response spectra. *Earthq. Spectra* **30**(3), 1117–1153.

Clevert, D.-A., T. Unterthiner, and S. Hochreiter (2016). Fast and accurate deep network learning by exponential linear units (elus). available at https://arxiv.org/abs/1511.07289 (last accessed April 2024).

Cornell, C. A. (1971). Probabilistic analysis of damage to structures under seismic loads. In D. A. Howells, P. Haigh, and C. Taylor (Eds.), *Dynamic Waves in Civil Engineering*, New York, pp. 473–488. Wiley.

Esfahani, R. D. D., F. Cotton, M. Ohrnberger, and F. Scherbaum (2022). TFCGAN: Nonstationary ground-motion simulation in the time–frequency domain using conditional generative adversarial network (cGAN) and phase retrieval methods. *Bull. Seismol. Soc. Am.* **113**(1), 453–467.

Esfahani, R. D. D., K. Vogel, F. Cotton, M. Ohrnberger, F. Scherbaum, and M. Kriegerowski (2021). Exploring the dimensionality of ground-motion data by applying autoencoder techniques. *Bull. Seismol. Soc. Am.* **111**(3), 1563–1576.

Federal Emergency Management Agency (FEMA) (2018). *FEMA P-58-1: Seismic Performance Assessment of Buildings, Volume 1 - Methodology*. Washington, DC.

Florez, M. A., M. Caporale, P. Buabthong, Z. E. Ross, D. Asimaki, and M. Meier (2022). Data-driven synthesis of broadband earthquake ground motions using artificial intelligence. *Bull. Seismol. Soc. Am.* **112**(4), 1979–1996.

Fujiwara, H., S. Kawai, S. Aoi, N. Morikawa, S. Senna, H. Azuma, M. Ooi, K. X. Hao, N. Hasegawa, T. Maeda, A. Iwaki, K. Wakamatsu, M. Imoto, T. Okumura, H. Matsuyama, and A. Narita (2012). Some improvements of seismic hazard assessment based on the 2011 Tohoku Earthquake. *Technical Note of the National Research Institute for Earth Science and Disaster Resilience* (379), 1–349. (in Japanese).

Fujiwara, H., N. Morikawa, T. Maeda, A. Iwaki, S. Senna, S. Kawai, H. Azuma, K. X. Hao, M. Imoto, K. Wakamatsu, J. Miyakoshi, T. Morii, N. Shimazu, M. Takahashi, and M. Akatsuka (2023). Improved seismic hazard assessment after the 2011 great east Japan earthquake (part 2). *Technical Note of the National Research Institute for Earth Science and Disaster Resilience*, 1–388.

Fukushima, Y. and T. Tanaka (1990). A new attenuation relation for peak horizontal acceleration of strong earthquake ground motion in Japan. *Bull. Seismol. Soc. Am.* **80**(4), 757–783.

Gardner, G. H. F., L. W. Gardner, and A. R. Gregory (1974). Formation velocity and density—the diagnostic basics for stratigraphic traps. *Geophysics* **39**(6), 770–780.

Gatti, F. and D. Clouteau (2020). Towards blending physics-based numerical simulations and seismic databases using generative adversarial network. *Comput. Meth. Appl. Mech. Eng.* **372**, 113421.

Ghofrani, H. and G. M. Atkinson (2014). Ground-motion prediction equations for interface earthquakes of M7 to M9 based on empirical data from Japan. *Bull. Earthq. Eng.* **12**(2), 549–571.

Goodfellow, I., Y. Bengio, and A. Courville (2016). *Deep Learning*. MIT Press. http://www.deeplearningbook.org.

Goodfellow, I. J., J. Pouget-Abadie, M. Mirza, B. Xu, D. Warde-Farley, S. Ozair, A. Courville, and Y. Bengio (2014). Generative adversarial networks. available at https://arxiv.org/abs/1406.2661 (last accessed April 2024).

Grijalva, F., W. Ramos, N. Pérez, D. Benítez, R. Lara-Cueva, and M. Ruiz (2021). ESeismic-GAN: A generative model for seismic events from cotopaxi volcano. *IEEE J. Sel. Top. Appl. Earth Obs. Remote Sens.* **14**, 7111–7120.

Gulrajani, I., F. Ahmed, M. Arjovsky, V. Dumoulin, and A. C. Courville (2017). Improved training of wasserstein gans. In *Adv. Neural Inf. Process. Syst.*, Volume 30.

Hancock, J. and J. J. Bommer (2006). A State-of-Knowledge review of the influence of Strong-Motion duration on structural damage. *Earthq. Spectra* **22**(3), 827–845.

He, K., X. Zhang, S. Ren, and J. Sun (2016). Deep residual learning for image recognition. In *Proc. IEEE Comput. Soc. Conf. Comput. Vis. Pattern Recognit.*, pp. 770–778.

Hikita, T. and Y. Tomozawa (2023). Variability of response spectra of single-path ground-motion record pairs. *Earthq. Spectra* **39**(4), 2470–2491.

Kameda, H. (1994). Probabilistic seismic hazard and stochastic ground motions. *Eng. Struct.* **16**(7), 547–557.

Kanno, T., A. Narita, N. Morikawa, H. Fujiwara, and Y. Fukushima (2006). A New Attenuation Relation for Strong Ground Motion in Japan Based on Recorded Data. *Bull. Seismol. Soc. Am.* **96**(3), 879–897.

Karras, T., T. Aila, S. Laine, and J. Lehtinen (2018). Progressive growing of gans for improved quality, stability, and variation. available at https://arxiv.org/abs/1710.10196 (last accessed April 2024).

Karras, T., S. Laine, and T. Aila (2021). A style-based generator architecture for generative adversarial networks. *IEEE Trans. Pattern Anal. Mach. Intell.* **43**(12), 4217–4228.

Karras, T., S. Laine, M. Aittala, J. Hellsten, J. Lehtinen, and T. Aila (2020). Analyzing and improving the image quality of stylegan. In *Proc. IEEE/CVF Comput. Soc. Conf. Comput. Vis. Pattern Recognit.*, pp. 8110–8119.

Kingma, D. P. and J. Ba (2017). Adam: A method for stochastic optimization. available at https://arxiv.org/abs/1412.6980 (last accessed April 2024).

Kuehn, N. M., Y. Bozorgnia, K. W. Campbell, and N. Gregor (2023). A regionalized partially nonergodic ground-motion model for subduction earthquakes using the NGA-Sub database. *Earthq. Spectra* **39**(3), 1625–1657.

Lavrentiadis, G., N. A. Abrahamson, K. M. Nicolas, Y. Bozorgnia, C. A. Goulet, A. Babič, J. Macedo, M. Dolšek, N. Gregor, A. R. Kottke, et al. (2023). Overview and introduction to development of non-ergodic earthquake ground-motion models. *Bull. Earthq. Eng.* **21**(11), 5121–5150.

Li, Y., B. Ku, G. Kim, J.-K. Ahn, and H. Ko (2020). Seismic signal synthesis by generative adversarial network with gated convolutional neural network structure. In *IGARSS 2020*, pp. 3857–3860.

Li, Y., B. Ku, S. Zhang, J.-K. Ahn, and H. Ko (2020). Seismic data augmentation based on conditional generative adversarial networks. *Sensors* **20**(23).

Lin, Y., T. Yeh, K. Ma, T. A. Song, S. Lee, B. Huang, and Y. Wu (2018). Source characteristics of the 2016 Meinong (ML 6.6), Taiwan, earthquake, revealed from dense seismic arrays: Double sources and pulse-like velocity ground motion. *Bull. Seismol. Soc. Am.* **108**(1), 188–199.

Luzi, L., Y. Dar, and R. Baraniuk (2021). Double descent and other interpolation phenomena in gans. available at https://arxiv.org/abs/2106.04003 (last accessed April 2024).

Maas, A. L., A. Y. Hannun, A. Y. Ng, et al. (2013). Rectifier nonlinearities improve neural network acoustic models. In *ICML*, Volume 30, pp. 3.

730 Matinfar, M., N. Khaji, and G. Ahmadi (2023). Deep convolutional generative adversarial networks for the generation of numerous artificial
731 spectrum-compatible earthquake accelerograms using a limited number of ground motion records. *Comput.-Aided Civ. Infrastruct.*
732 *Eng.* **38**(2), 225–240.
733 Matsumoto, Y., T. Yaoyama, S. Lee, T. Hida, and T. Itoi (2023). Fundamental study on probabilistic generative modeling of earthquake
734 ground motion time histories using generative adversarial networks. *Jpn. Archit. Rev.* **6**(1), e12392.
735 McInnes, L., J. Healy, and J. Melville (2020). Umap: Uniform manifold approximation and projection for dimension reduction. available
736 at https://arxiv.org/abs/1802.03426 (last accessed July 2024).
737 Mescheder, L., A. Geiger, and S. Nowozin (2018). Which training methods for GANs do actually converge? In *ICML*, Volume 80, pp.
738 3481–3490.
739 Mirza, M. and S. Osindero (2014). Conditional generative adversarial nets. available at https://arxiv.org/abs/1411.1784 (last accessed April
740 2024).
741 Miyato, T. and M. Koyama (2018). cgans with projection discriminator. available at https://arxiv.org/abs/1802.05637 (last accessed April
742 2024).
743 Molas, G. L. and F. Yamazaki (1995). Attenuation of earthquake ground motion in Japan including deep focus events. *Bull. Seismol. Soc.*
744 *Am.* **85**(5), 1343–1358.
745 Morikawa, N. and H. Fujiwara (2013). A new ground motion prediction equation for Japan applicable up to M9 mega-earthquake. *J.*
746 *Disaster Res.* **8**(5), 878–888.
747 Morikawa, N., T. Kanno, A. Narita, H. Fujiwara, T. Okumura, Y. Fukushima, and A. Guerpinar (2008). Strong motion uncertainty
748 determined from observed records by dense network in japan. *J. Seismol.* **12**, 529–546.
749 Naeim, F., A. Alimoradi, and S. Pezeshk (2004). Selection and scaling of ground motion time histories for structural design using genetic
750 algorithms. *Earthq. Spectra* **20**(2), 413–426.
751 Nakajima, J. and T. Matsuzawa (2017). Anelastic properties beneath the niigata–kobe tectonic zone, Japan. *Earth, Planets and Space* **69**.
752 Nakamura, R. and T. Uetake (2002). Three dimensional attenuation structure and site amplification inversionby using a large quantity of
753 seismic strong motion records in Japan. *Zisin (Journal of the Seismological Society of Japan. 2nd ser.)* **54**(4), 475–488. (in Japanese with
754 English abstract).
755 National Institute of Advanced Industrial Science and Technology (2024). Active Fault Database of Japan, April 26, 2024
756 version. GSJ Database, Geological Survey of Japan, National Institute of Advanced Industrial Science and Technology.
757 https://gbank.gsj.jp/activefault/index_e_gmap.html (last accessed July 2024).
758 National Research Institute for Earth Science and Disaster Resilience (2019a). NIED J-SHIS. National Research Institute for Earth Science
759 and Disaster Resilience, https://doi.org/10.17598/nied.0010.
760 National Research Institute for Earth Science and Disaster Resilience (2019b). NIED K-NET, KiK-net. National Research Institute for
761 Earth Science and Disaster Resilience, doi:10.17598/NIED.0004.
762 National Research Institute for Earth Science and Disaster Resilience (2024). NIED F-net. available at
763 https://www.fnet.bosai.go.jp/top.php?LANG=ja (last accessed April 2024).

764 Nishimura, T. and M. Horike (2003). The attenuation relationships of peak ground acceleration for the horizontal and the vertical
765 components inferred from the Kyoshin network data. *J. Struct. Constr. Eng.* **571**, 63–70. (in Japanese with English abstract).
766 Parker, G. A., J. P. Stewart, D. M. Boore, G. M. Atkinson, and B. Hassani (2022). NGA-subduction global ground motion models with
767 regional adjustment factors. *Earthq. Spectra* **38**(1), 456–493.
768 Paszke, A., S. Gross, F. Massa, A. Lerer, J. Bradbury, G. Chanan, T. Killeen, Z. Lin, N. Gimelshein, L. Antiga, A. Desmaison, A. Kopf,
769 E. Yang, Z. DeVito, M. Raison, A. Tejani, S. Chilamkurthy, B. Steiner, L. Fang, J. Bai, and S. Chintala (2019). Pytorch: An imperative
770 style, high-performance deep learning library. In H. Wallach, H. Larochelle, A. Beygelzimer, F. d'Alché-Buc, E. Fox, and R. Garnett
771 (Eds.), *Adv. Neural Inf. Process. Syst.*, Volume 32.
772 Pitarka, A., K. Irikura, T. Iwata, and H. Sekiguchi (1998). Three-dimensional simulation of the near-fault ground motion for the 1995
773 Hyogo-Ken Nanbu (Kobe), Japan, earthquake. *Bull. Seismol. Soc. Am.* **88**(2), 428–440.
774 Radford, A., L. Metz, and S. Chintala (2016). Unsupervised representation learning with deep convolutional generative adversarial
775 networks. available at https://arxiv.org/abs/1511.06434 (last accessed April 2024).
776 Rahman, M. A., M. A. Florez, A. Anandkumar, Z. E. Ross, and K. Azizzadenesheli (2022). Generative adversarial neural operators. *TMLR*.
777 Rezaeian, S. and A. Der Kiureghian (2008). A stochastic ground motion model with separable temporal and spectral nonstationarities.
778 *Earthq. Eng. Struct. Dynam.* **37**(13), 1565–1584.
779 Rezaeian, S. and A. Der Kiureghian (2010). Simulation of synthetic ground motions for specified earthquake and site characteristics.
780 *Earthq. Eng. Struct. Dynam.* **39**(10), 1155–1180.
781 Ruthotto, L. and E. Haber (2021). An introduction to deep generative modeling. *GAMM-Mitteilungen* **44**(2), e202100008.
782 Shi, Y., G. Lavrentiadis, D. Asimaki, Z. E. Ross, and K. Azizzadenesheli (2024). Broadband ground motion synthesis via generative
783 adversarial neural operators: Development and validation. available at https://arxiv.org/abs/2309.03447 (last accessed April 2024).
784 Si, H. and S. Midorikawa (1999). New attenuation relationships for peak ground acceleration and velocity considering effects of fault type
785 and site condition. *J. Struct. Constr. Eng.* **523**, 63–70. (in Japanese with English abstract).
786 Si, H., S. Midorikawa, and T. Kishida (2022). Development of nga-sub ground-motion prediction equation of 5%-damped pseudo-spectral
787 acceleration based on database of subduction earthquakes in japan. *Earthq. Spectra* **38**(4), 2682–2706.
788 Sung, C., H. Miyake, N. Abrahamson, and N. Morikawa (2024). Nonergodic Ground-Motion Models for Subduction Zone and Crustal
789 Earthquakes in Japan. *Bull. Seismol. Soc. Am.*.
790 Tavaré, S., D. J. Balding, R. C. Griffiths, and P. Donnelly (1997). Inferring coalescence times from DNA sequence data. *Genetics* **145**(2),
791 505–518.
792 Trifunac, M. D. and A. G. Brady (1975). A study on the duration of strong earthquake ground motion. *Bull. Seismol. Soc. Am.* **65**(3), 581–626.
793 Vamvatsikos, D. and C. A. Cornell (2002). Incremental dynamic analysis. *Earthq. Eng. Struct. Dynam.* **31**(3), 491–514.
794 Wang, T., D. Trugman, and Y. Lin (2021). Seismogen: Seismic waveform synthesis using gan with application to seismic data augmentation.
795 *J. Geophys. Res. Solid Earth* **126**(4), e2020JB020077.
796 Wang, T., Z. Zhang, and Y. Li (2019). EarthquakeGen: Earthquake generator using generative adversarial networks. SEG Int. Expo. Annu.
797 Meet., pp. D043S119R004.

Wang, Y., L. K. Sambasivan, M. Fu, and P. Mehrotra (2024). Pivoting retail supply chain with deep generative techniques: Taxonomy, survey and insights. available at https://arxiv.org/abs/2403.00861 (last accessed April 2024).

Wiemer, S. and M. Wyss (2000). Minimum magnitude of completeness in earthquake catalogs: Examples from Alaska, the western United States, and Japan. *Bulletin of the Seismological Society of America* **90**(4), 859–869.

Zhao, J. X., J. Zhang, A. Asano, Y. Ohno, T. Oouchi, T. Takahashi, H. Ogawa, K. Irikura, H. K. Thio, P. G. Somerville, Y. Fukushima, and Y. Fukushima (2006). Attenuation relations of strong ground motion in Japan using site classification based on predominant period. *Bull. Seismol. Soc. Am.* **96**(3), 898–913.

Zhao, J. X., S. Zhou, J. Zhou, C. Zhao, H. Zhang, Y. Zhang, P. Gao, X. Lan, D. Rhoades, Y. Fukushima, P. G. Somerville, and K. Irikura (2016). Ground-motion prediction equations for shallow crustal and upper-mantle earthquakes in Japan using site class and simple geometric attenuation functions. *Bull. Seismol. Soc. Am.* **106**(4), 1552–1569.

Zhu, C., F. Cotton, H. Kawase, and K. Nakano (2023). How well can we predict earthquake site response so far? Machine learning vs physics-based modeling. *Earthquake Spectra* **39**(1), 478–504.

Postal mailing address for each author

- Yuma Matsumoto: Department of Architecture, Graduate School of Engineering, The University of Tokyo, 7-3-1 Hongo, Bunkyo-ku, Tokyo, 1138656, Japan.
- Taro Yaoyama: Department of Architecture, Graduate School of Engineering, The University of Tokyo, 7-3-1 Hongo, Bunkyo-ku, Tokyo, 1138656, Japan.
- Sangwon Lee: Department of Architecture, Graduate School of Engineering, The University of Tokyo, 7-3-1 Hongo, Bunkyo-ku, Tokyo, 1138656, Japan.
- Takenori Hida: Major in Urban and Civil Engineering, Graduate School of Science and Engineering, Ibaraki University, 4-12-1, Nakanarusawa-cho, Hitachi-shi, Ibaraki, 316-8511, Japan.
- Tatsuya Itoi: Department of Architecture, Graduate School of Engineering, The University of Tokyo, 7-3-1 Hongo, Bunkyo-ku, Tokyo, 1138656, Japan.

List of figure captions

- Figure 1. Map of the training dataset showing the locations of the earthquake epicenters (circles) and stations (triangles).
- Figure 2. Magnitude-distance distribution of the compiled training dataset.
- Figure 3. Diagram of overall architecture of the GMGM.
- Figure 4. Diagram of the neural network architecture of the proposed GMGM. (a) is the generator, and (b) is the discriminator.
- Figure 5. Examples of the ground motion waveforms of observed records. The data in each column correspond to the value of M_W shown at the top. Each panel shows the associated R_{RUP} and V_{S30} values.
- Figure 6. Examples of the ground motion waveforms generated by the GMGM. The data in each column correspond to the value of M_W shown at the top. Each panel shows the associated R_{RUP} and V_{S30} values.
- Figure 7. Comparison of the cumulative distribution functions (CDF) for five indices of ground motions. The blue dashed line is the CDF of observed records, and red solid line is the CDF of generated ground motions.
- Figure 8. Comparison of the condition label distributions between observed records and generated data. (a) Rupture distance and moment magnitude, (b) moment magnitude and PGA, (c) rupture distance and PGA, (d) V_{S5} and V_{S10}, (e) V_{S10} and V_{S20}, (f) V_{S20} and $Z_{1.0}$, (g) $Z_{1.0}$ and $Z_{1.4}$, and (h) M_W and V_{S30}. In each case, the left side represents the distribution of observed records, and the right side represents the distribution of generated data.
- Figure 9. The distribution of latent variables $\mathbf{w}$ reduced to two-dimensional data using UMAP. Each dot corresponds to a sample of the generated data, and is color coded according to the values of (a) Arias intensity, (b) moment magnitude, and (c) rupture distance.
- Figure 10. Comparison of the CDF of the pulse indicator values. The blue dashed line represents the observed records, and red solid line represents the generated ground motions.
- Figure 11. Examples of the velocity waveforms and their corresponding extracted pulses. The left column is the observed record and right column is the generated ground motion. The scenario M_W, R_{RUP}, and V_{S30} of each data is shown at the top of each column.
- Figure 12. Comparison of the logarithmic means and logarithmic standard deviations of the FAS across three different M_W ranges (a-c). Panels (a), (b), and (c) have three different R_{RUP} and V_{S30} scenarios, respectively. For each panel, the blue dashed line corresponds to observed records, and the red solid line corresponds to generated ground motions.
- Figure 13. Comparison of the 5% damped spectral acceleration values at periods $T = 0.2$ s and 1.0 s between the generated ground motions and prediction results from the empirical GMMs. (a) represents the comparison results with the MF13 GMM across three different M_W, R_{RUP}, V_{S30}, and $Z_{1.4}$ scenarios. (b) represents the comparison results with the ASK14 GMM across three different M_W, R_{RUP}, V_{S30}, and $Z_{1.0}$ scenarios. The purple circles represents the generated ground

motions, the blue solid line represents the median of the GMMs prediction, and the blue dashed line represents the ±1 standard deviation interval. The corresponding values of M_W and soil conditions are shown at the top of each panel.

- Figure 14. Residual plots between the 5% damped spectral acceleration of ground motions generated by the GMGM and the median predictions of the MF13 GMM. Grey circles represent the residuals for each generated data, blue squares indicate the mean, and orange bars show the median along with the 16th and 84th percentiles. Each panel represents the residuals for a period of $T = 0.2$ s on the left and $T = 1.0$ s on the right.
- Figure 15. Residual plots between the 5% damped spectral acceleration of ground motions generated by the GMGM and the median predictions of the ASK14 GMM. Grey circles represent the residuals for each generated data, blue squares indicate the mean, and orange bars show the median along with the 16th and 84th percentiles. Each panel represents the residuals for a period of $T = 0.2$ s on the left and $T = 1.0$ s on the right.
- Figure 16. Examples of ground motion waveforms, FAS, shear-wave velocity profiles of generated data with almost same M_W, R_{RUP}, and V_{S30} values.
- Figure 17. The distribution of the generated ground motions with almost same magnitude, distance, and site conditions scenarios. Panel (a) represents the means and standard deviations (in natural log units) of 5% damped acceleration spectra for three scenarios. The black solid line with circles represent the distribution of generated acceleration spectra with specified values of M_W, R_{RUP}, and V_{S30}. The red dashed line with squares (Case 1) and blue dotted line with triangles (Case 2) indicate the mean acceleration spectra of generated ground motions, which include additional specifications of the shear-wave velocity profiles along with the aforementioned M_W, R_{RUP}, and V_{S30}. The standard deviations for Case 1 and Case 2 are calculated together to ensure a sufficient sample size and are represented by a green dashed line with inverted triangles. Panel (b) represents the corresponding shear-wave velocity profiles for each generated data of the three scenarios. Panel (c) shows the logarithmic mean of the FAS of the generated ground motions for Case 1 and Case 2 (represented by red and blue solid lines, respectively), along with the amplification spectra (represented by the purple dashed lines) derived from the shear-wave velocity profiles in Panel (b).
- Figure 18. The locations of the YMG007 K-NET station (triangle) and earthquake epicenters (circles) whose ground motions were observed at YMG007 station and contained in our training dataset. The focal mechanisms were obtained from F-net database.
- Figure 19. Magnitude-distance distribution of the observed records at YMG007 K-NET station (blue circle) and generated ground motions (red cross) with site conditions similar to YMG007 station.
- Figure 20. Ground motion waveforms (a), their corresponding acceleration spectra (b), and shear-wave velocity profiles (c) that satisfy the condition 42 km $\leq R_{RUP} \leq$ 44 km in Figure 19. The blue solid line represents the observed record at the YMG007 K-NET station, and red dashed line represent the generated data. The shear-wave velocity profile of the YMG007

station was modeled with three layers based on the P-S logging data of the K-NET database. All condition label values for the data shown in this figure are distributed within the range indicated at the top of the figure.

- Figure 21. Locations of the epicenter of the earthquake and the target KiK-net stations TCGH07, NGNH26, and NIGH11. The focal mechanism of the earthquake was obtained from the F-net database. The green lines represent the active segments of the Itoigawa–Shizuoka Tectonic Line (ISTL) obtained from the Active Fault Database of Japan (National Institute of Advanced Industrial Science and Technology, 2024).
- Figure 22. Comparison of shear-wave velocity profiles (left panels) and 5% damped response spectra (right panels) of the observed records versus generated ground motions for the target KiK-net stations: (a) TCGH07, (b) NGNH26, and (c) NIGH11. The blue solid lines represent the observed records, the red dashed lines represent the generated data, the green dash-dot lines represent the median of the MF13 GMM predictions, and the green dotted lines represent the ± 1 standard deviation interval of the MF13 GMM predictions.
- Figure 23. An example of generated ground motion waveform with subsequent oscillations showing large amplitude noise. The values at the top of this figure represent the corresponding condition label values.

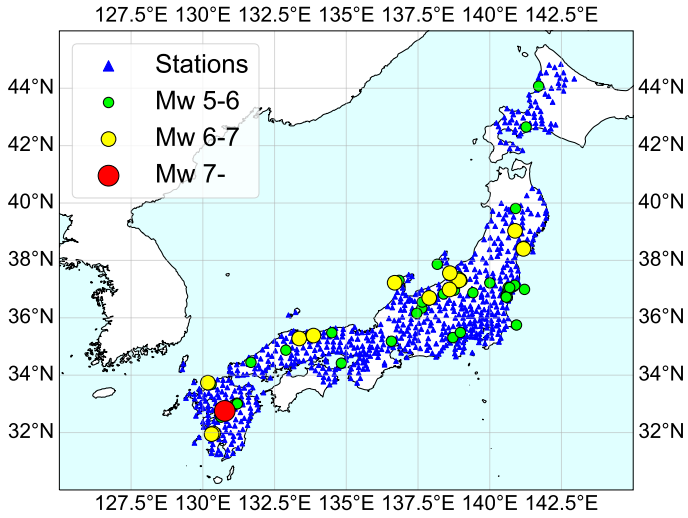

Figure 1. Map of the training dataset showing the locations of the earthquake epicenters (circles) and stations (triangles).

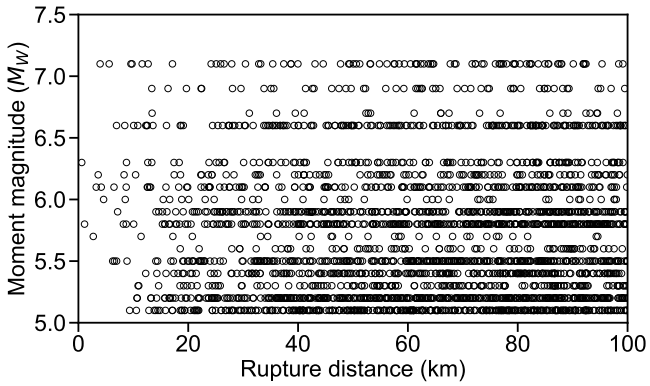

Figure 2. Magnitude-distance distribution of the compiled training dataset.

896

Manuscript Received 00 Month 0000

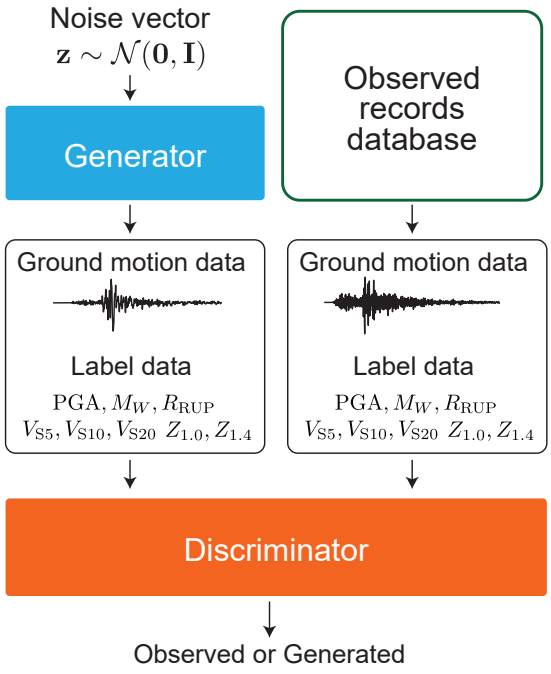

Figure 3. Diagram of overall architecture of the GMGM.

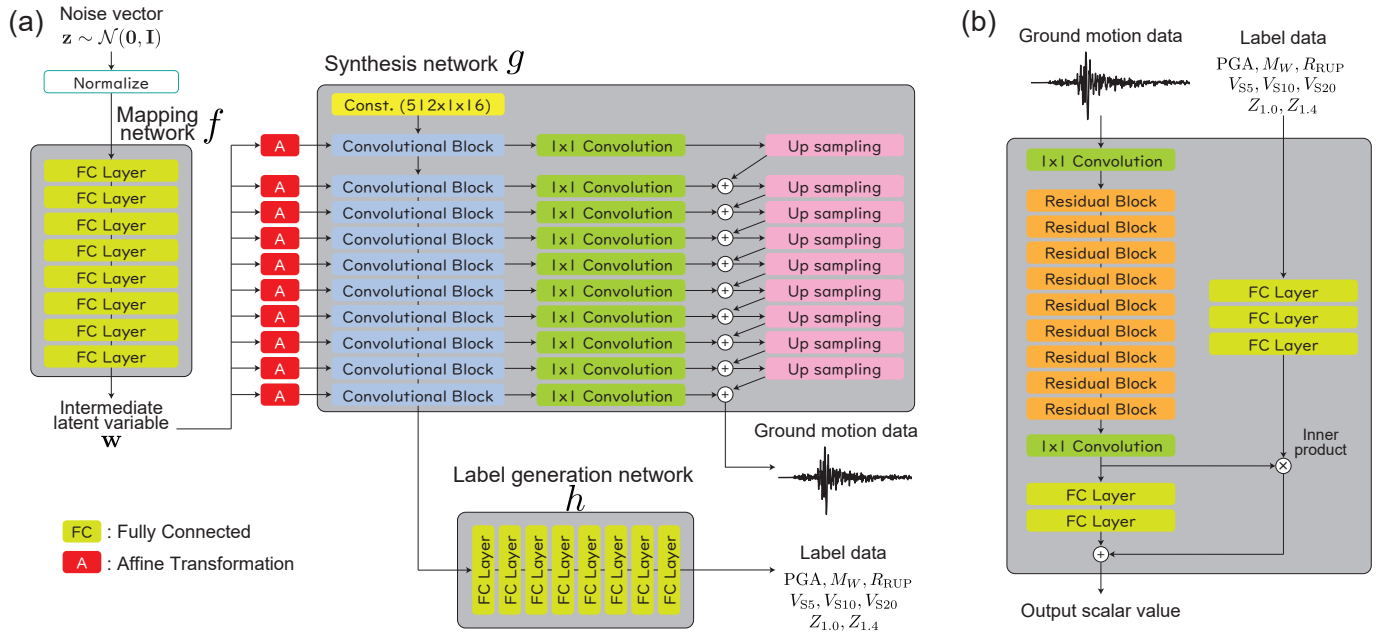

Figure 4. Diagram of the neural network architecture of the proposed GMGM. (a) is the generator, and (b) is the discriminator.

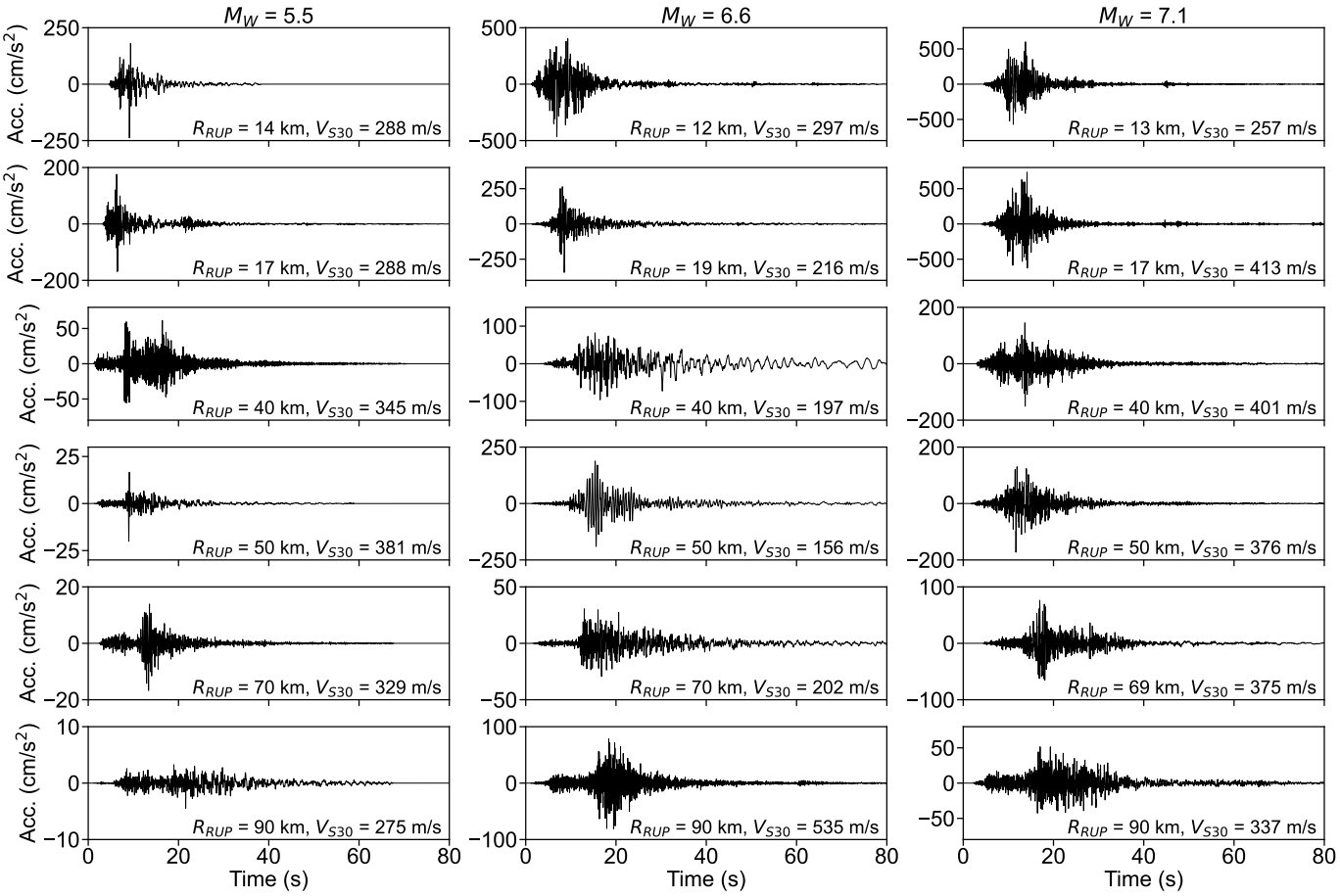

Figure 5. Examples of the ground motion waveforms of observed records. The data in each column correspond to the value of M_W shown at the top. Each panel shows the associated R_{RUP} and V_{S30} values.

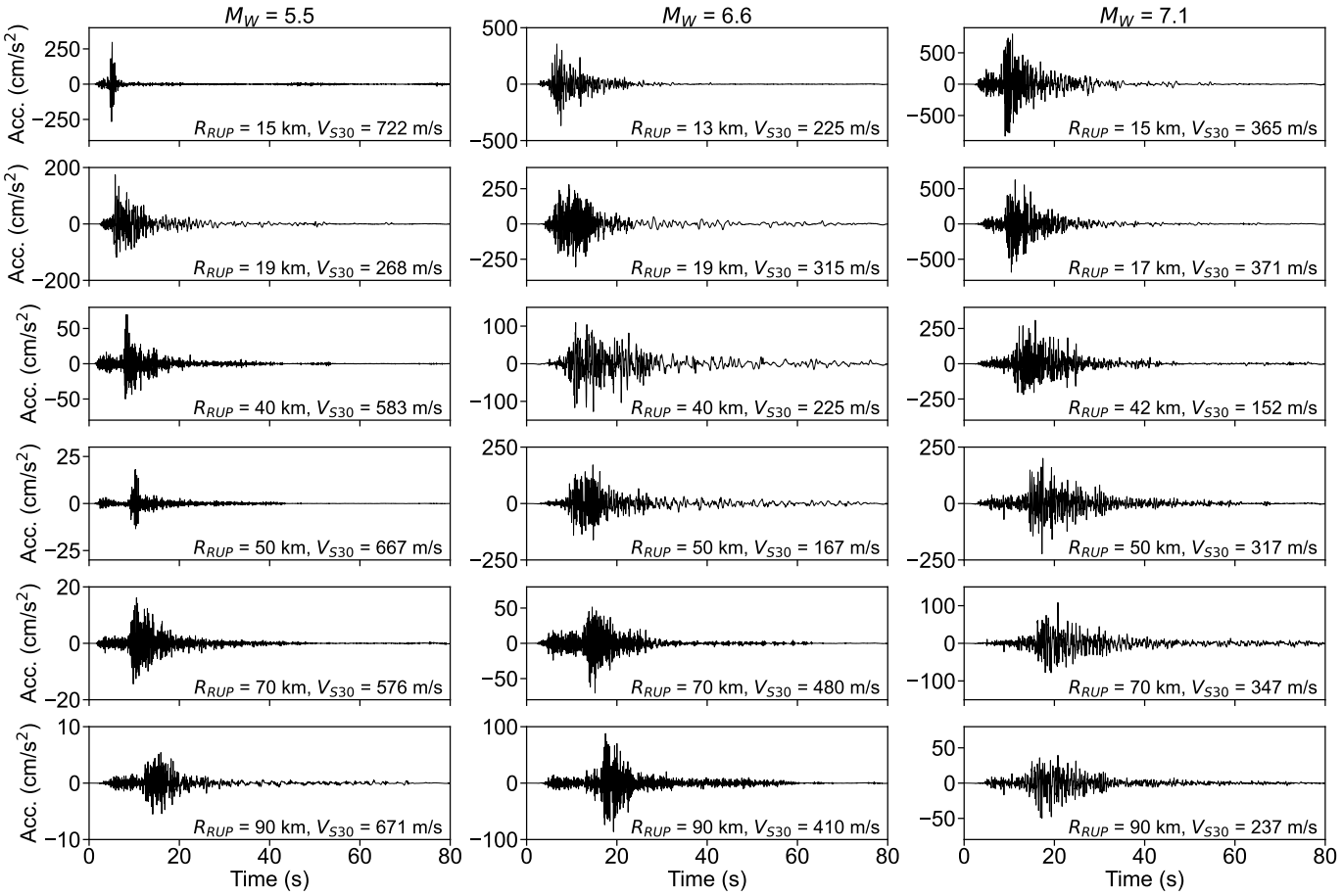

Figure 6. Examples of the ground motion waveforms generated by the GMGM. The data in each column correspond to the value of M_W shown at the top. Each panel shows the associated R_{RUP} and V_{S30} values.

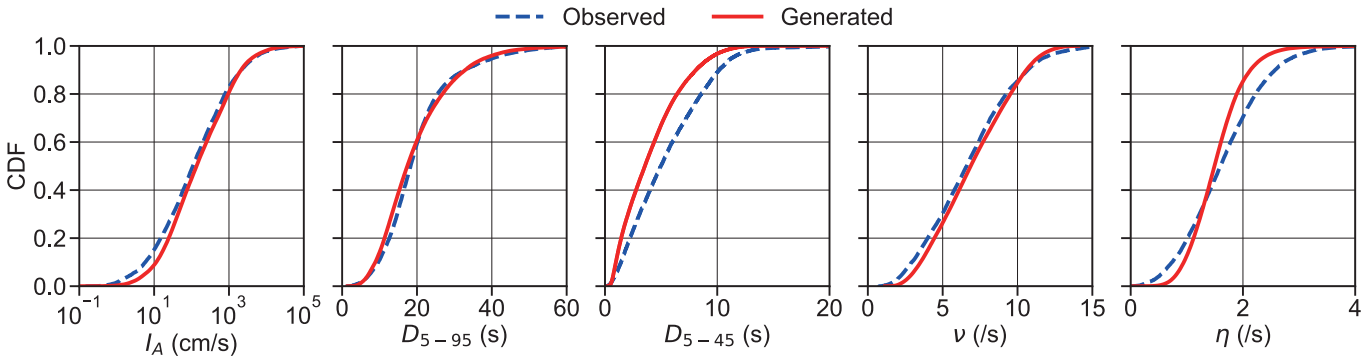

Figure 7. Comparison of the cumulative distribution functions (CDF) for five indices of ground motions. The blue dashed line is the CDF of observed records, and red solid line is the CDF of generated ground motions.

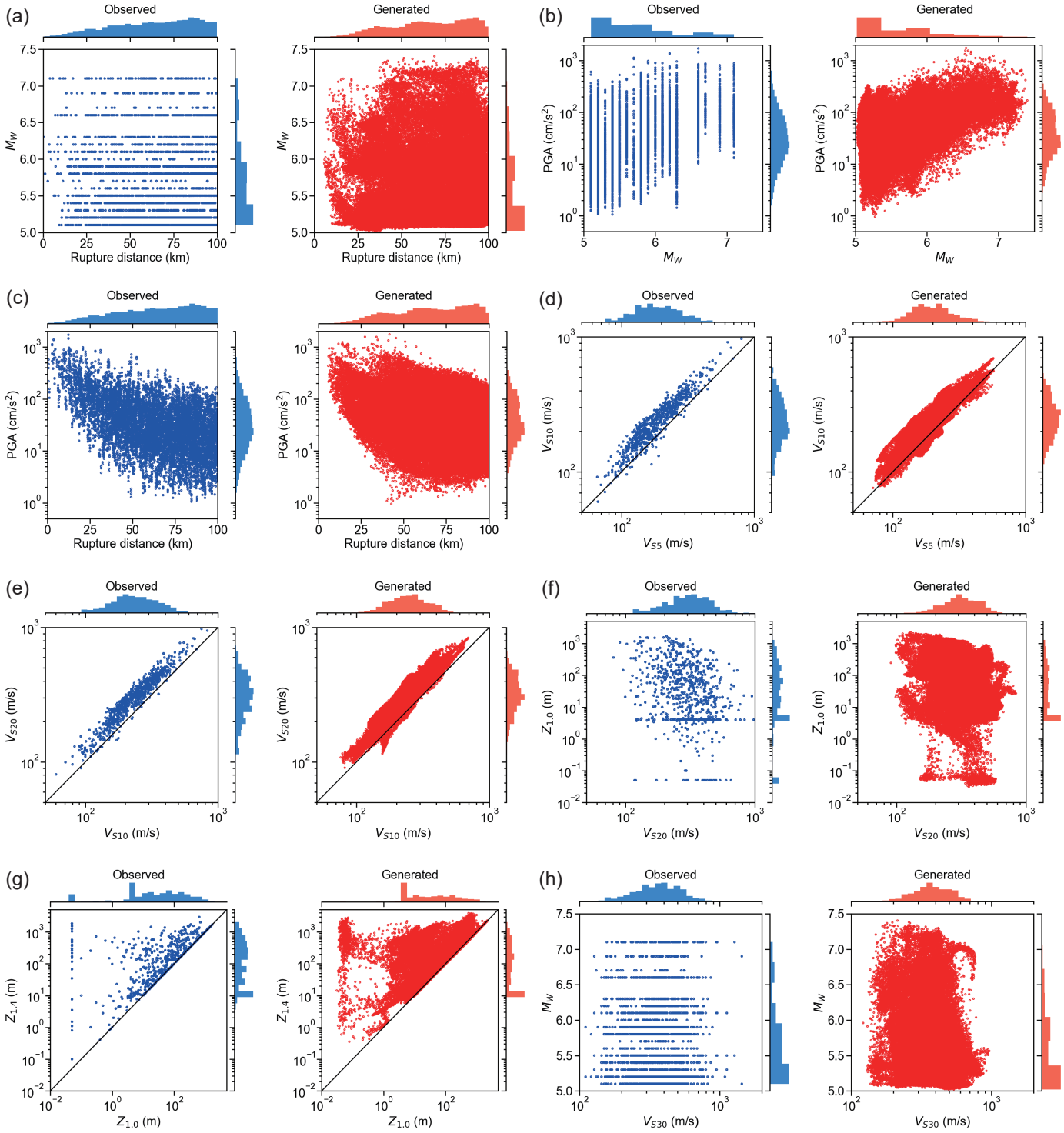

Figure 8. Comparison of the condition label distributions between observed records and generated data. (a) Rupture distance and moment magnitude, (b) moment magnitude and PGA, (c) rupture distance and PGA, (d) V_{S5} and V_{S10}, (e) V_{S10} and V_{S20}, (f) V_{S20} and $Z_{1.0}$, (g) $Z_{1.0}$ and $Z_{1.4}$, and (h) M_W and V_{S30}. In each case, the left side represents the distribution of observed records, and the right side represents the distribution of generated data.

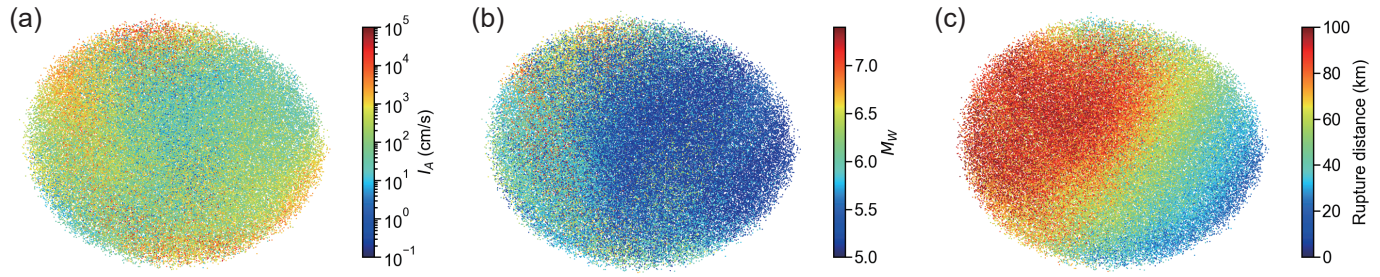

Figure 9. The distribution of latent variables $\mathbf{w}$ reduced to two-dimensional data using UMAP. Each dot corresponds to a sample of the generated data, and is color coded according to the values of (a) Arias intensity, (b) moment magnitude, and (c) rupture distance.

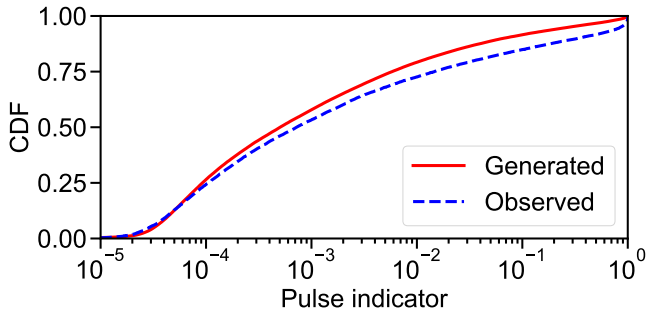

Figure 10. Comparison of the CDF of the pulse indicator values. The blue dashed line represents the observed records, and red solid line represents the generated ground motions.

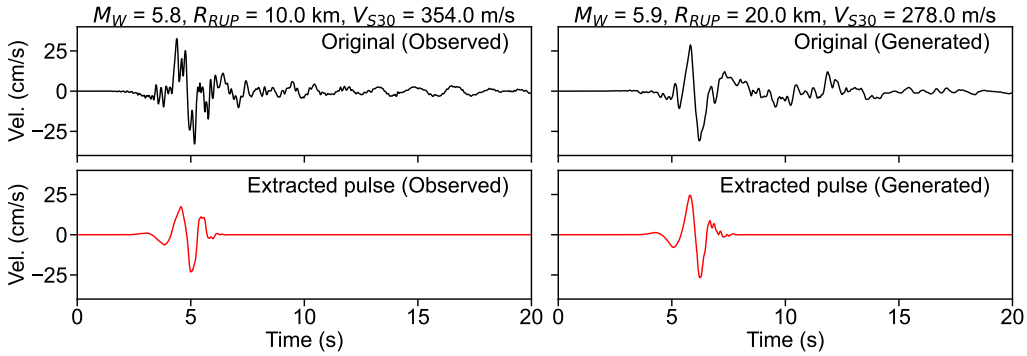

Figure 11. Examples of the velocity waveforms and their corresponding extracted pulses. The left column is the observed record and right column is the generated ground motion. The scenario M_W, R_{RUP}, and V_{S30} of each data is shown at the top of each column.

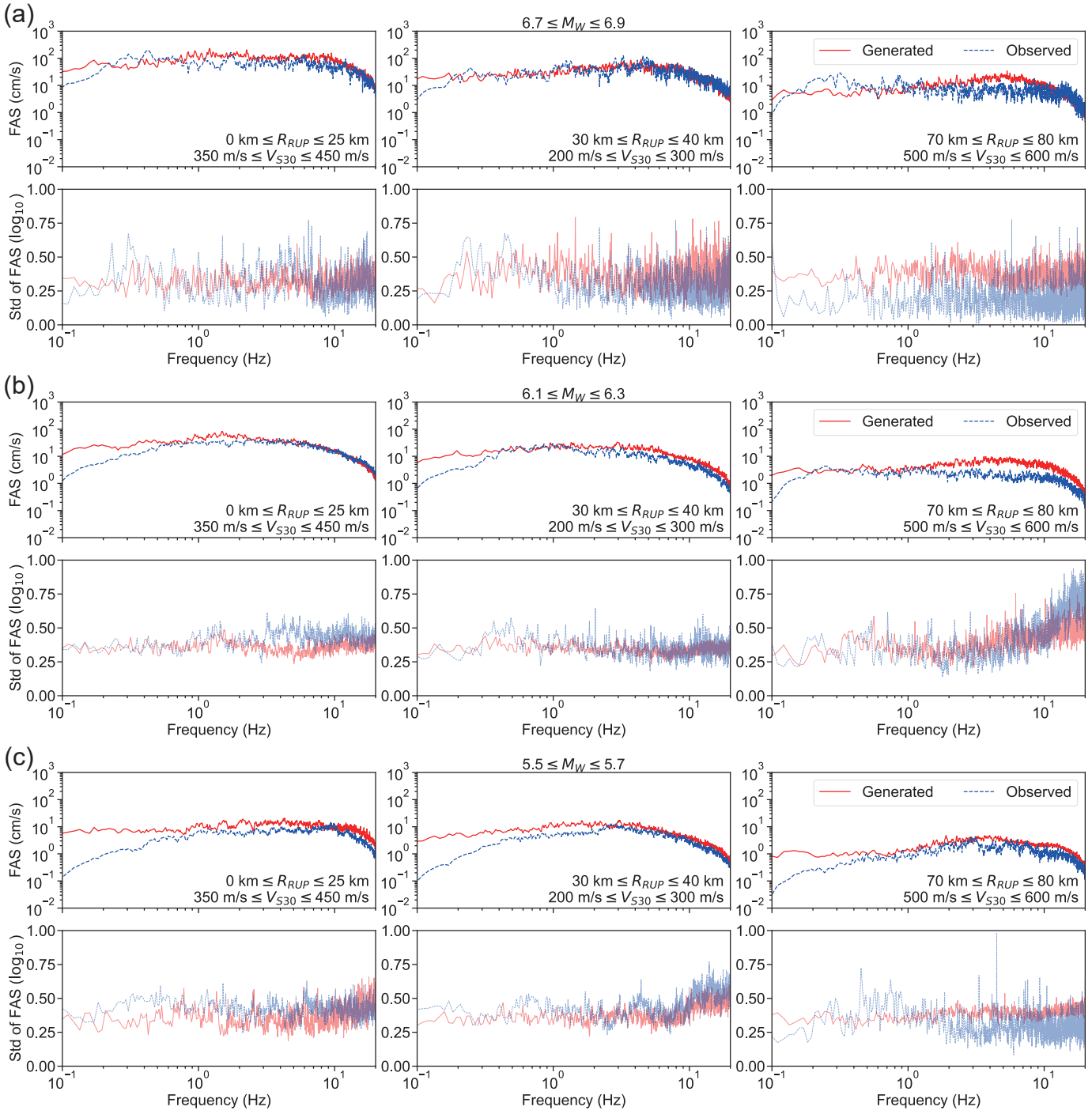

Figure 12. Comparison of the logarithmic means and logarithmic standard deviations of the FAS across three different M_W ranges (a-c). Panels (a), (b), and (c) have three different R_{RUP} and V_{S30} scenarios, respectively. For each panel, the blue dashed line corresponds to observed records, and the red solid line corresponds to generated ground motions.

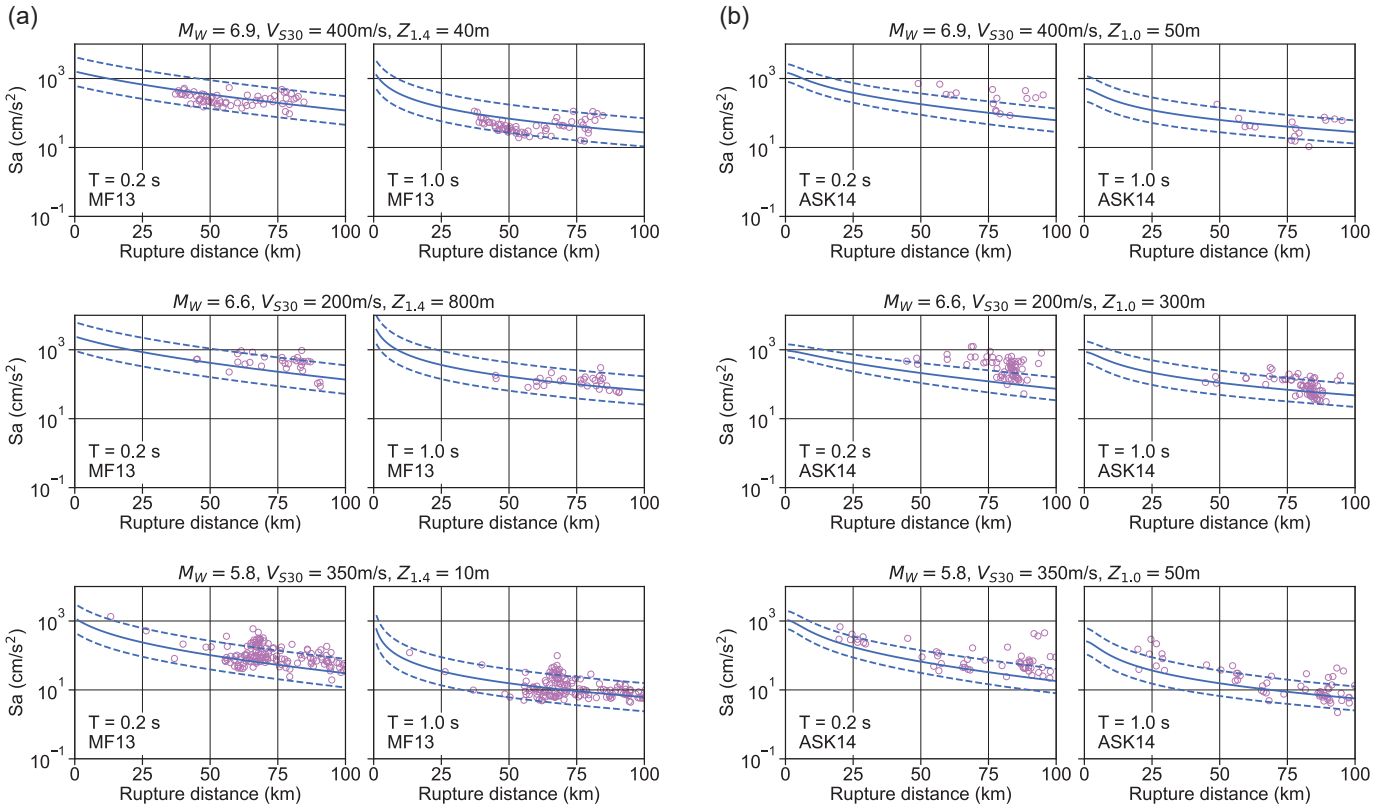

Figure 13. Comparison of the 5% damped spectral acceleration values at periods $T = 0.2$ s and 1.0 s between the generated ground motions and prediction results from the empirical GMMs. (a) represents the comparison results with the MF13 GMM across three different M_W, R_{RUP}, V_{S30}, and $Z_{1.4}$ scenarios. (b) represents the comparison results with the ASK14 GMM across three different M_W, R_{RUP}, V_{S30}, and $Z_{1.0}$ scenarios. The purple circles represents the generated ground motions, the blue solid line represents the median of the GMMs prediction, and the blue dashed line represents the ± 1 standard deviation interval. The corresponding values of M_W and soil conditions are shown at the top of each panel.

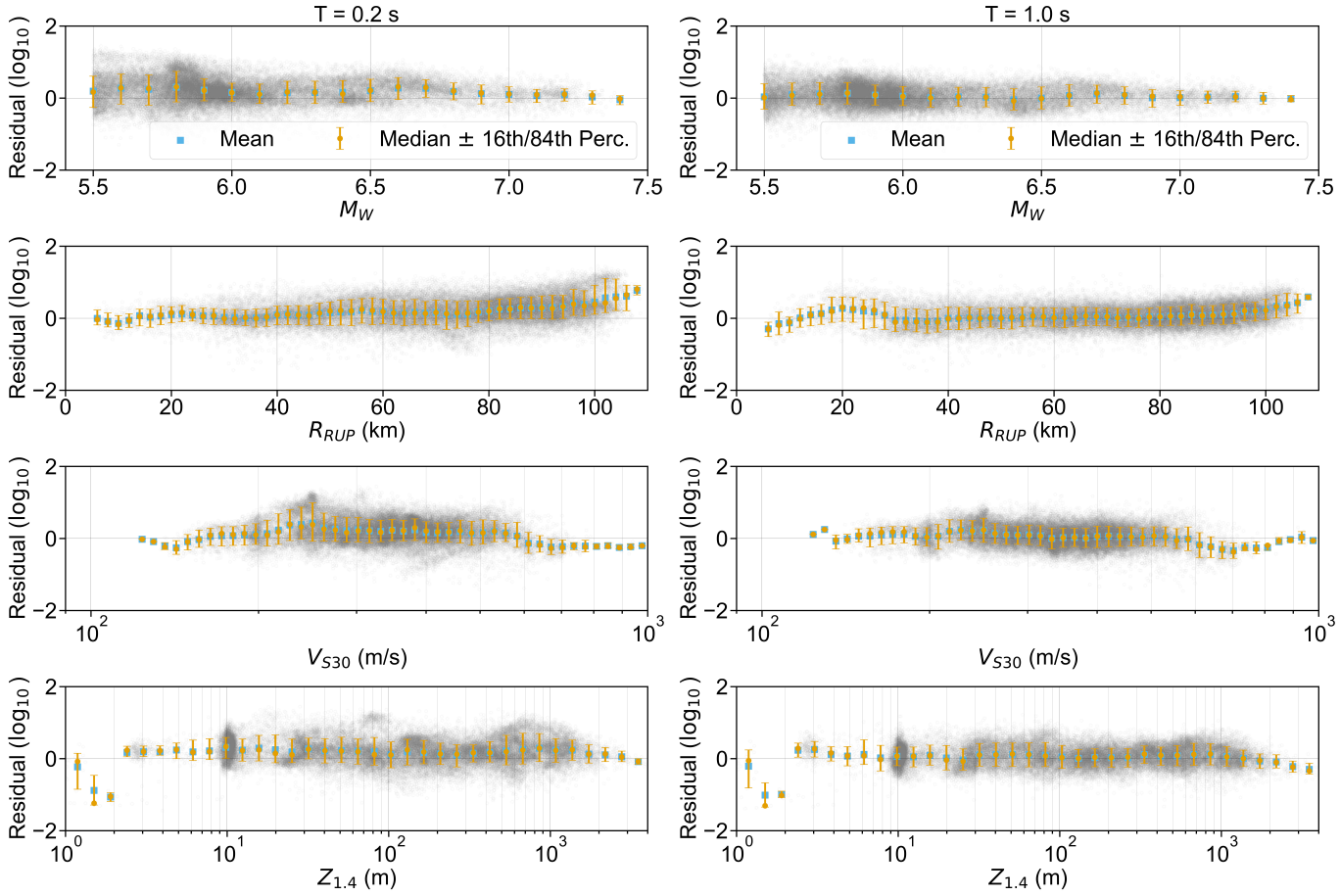

Figure 14. Residual plots between the 5% damped spectral acceleration of ground motions generated by the GMGM and the median predictions of the MF13 GMM. Grey circles represent the residuals for each generated data, blue squares indicate the mean, and orange bars show the median along with the 16th and 84th percentiles. Each panel represents the residuals for a period of $T = 0.2$ s on the left and $T = 1.0$ s on the right.

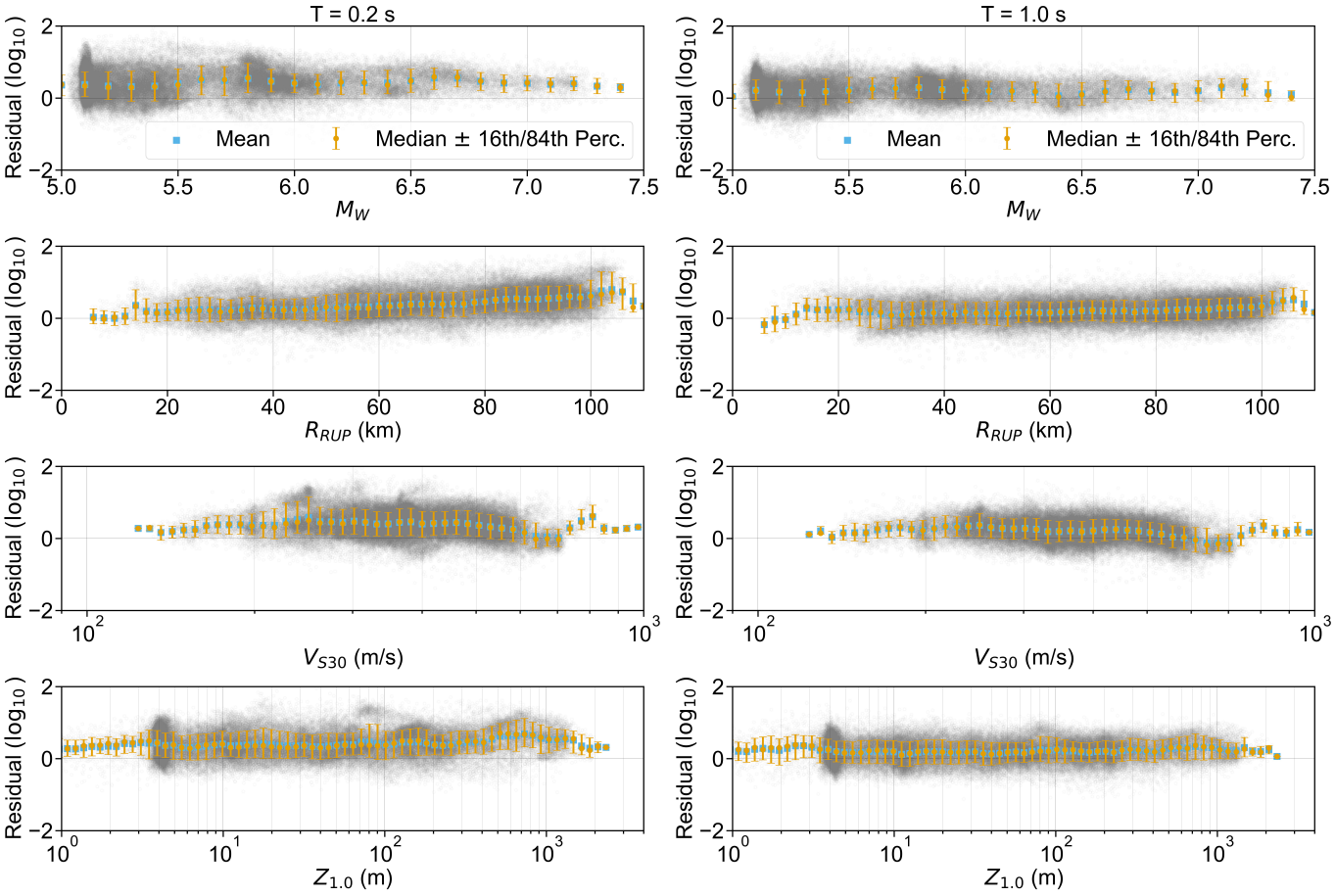

Figure 15. Residual plots between the 5% damped spectral acceleration of ground motions generated by the GMGM and the median predictions of the ASK14 GMM. Grey circles represent the residuals for each generated data, blue squares indicate the mean, and orange bars show the median along with the 16th and 84th percentiles. Each panel represents the residuals for a period of $T = 0.2$ s on the left and $T = 1.0$ s on the right.

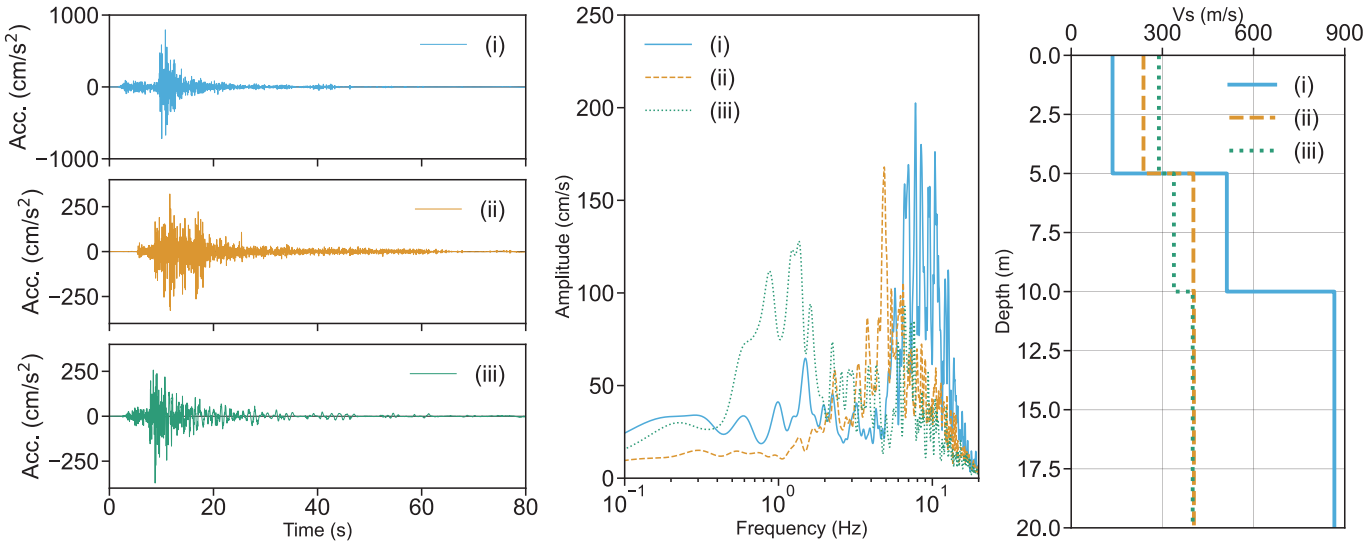

Figure 16. Examples of ground motion waveforms, FAS, shear-wave velocity profiles of generated data with almost same M_W, R_{RUP}, and V_{S30} values.

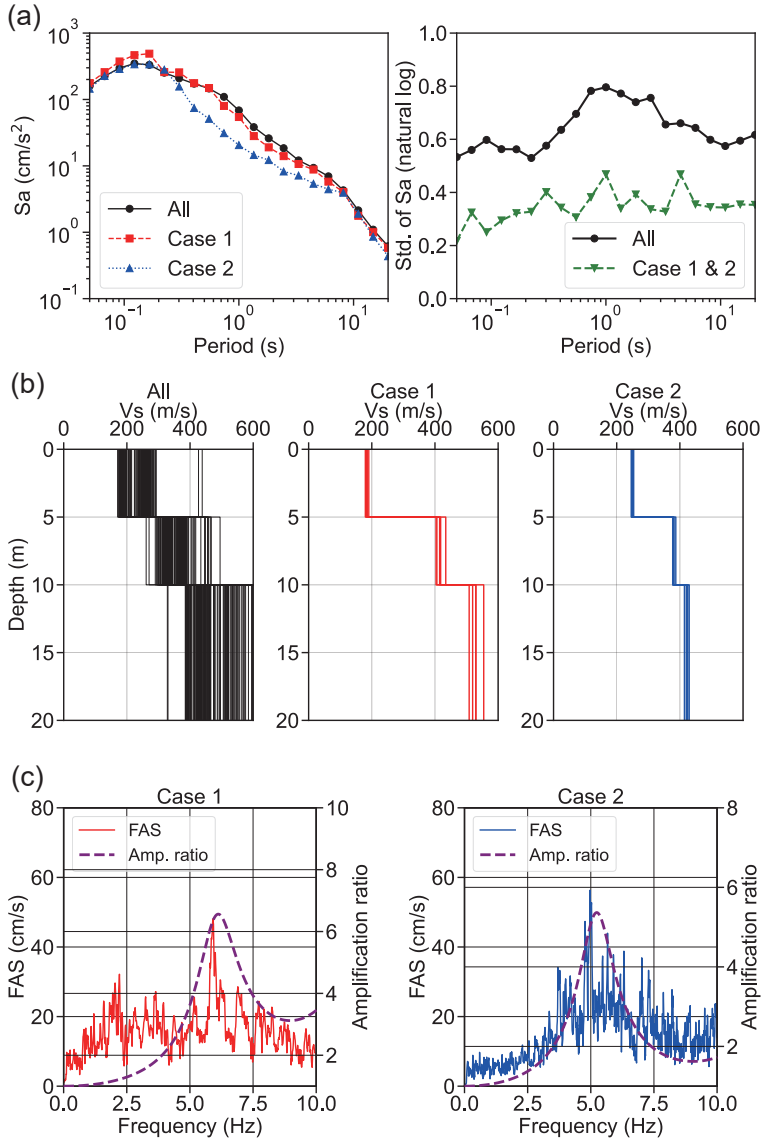

Figure 17. The distribution of the generated ground motions with almost same magnitude, distance, and site conditions scenarios. Panel (a) represents the means and standard deviations (in natural log units) of 5% damped acceleration spectra for three scenarios. The black solid line with circles represent the distribution of generated acceleration spectra with specified values of M_W, R_{RUP}, and V_{S30}. The red dashed line with squares (Case 1) and blue dotted line with triangles (Case 2) indicate the mean acceleration spectra of generated ground motions, which include additional specifications of the shear-wave velocity profiles along with the aforementioned M_W, R_{RUP}, and V_{S30}. The standard deviations for Case 1 and Case 2 are calculated together to ensure a sufficient sample size and are represented by a green dashed line with inverted triangles. Panel (b) represents the corresponding shear-wave velocity profiles for each generated data of the three scenarios. Panel (c) shows the logarithmic mean of the FAS of the generated ground motions for Case 1 and Case 2 (represented by red and blue solid lines, respectively), along with the amplification spectra (represented by the purple dashed lines) derived from the shear-wave velocity profiles in Panel (b).

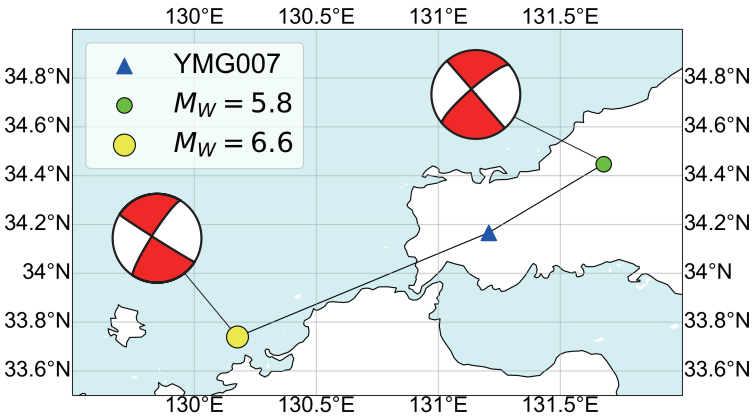

Figure 18. The locations of the YMG007 K-NET station (triangle) and earthquake epicenters (circles) whose ground motions were observed at YMG007 station and contained in our training dataset. The focal mechanisms were obtained from F-net database.

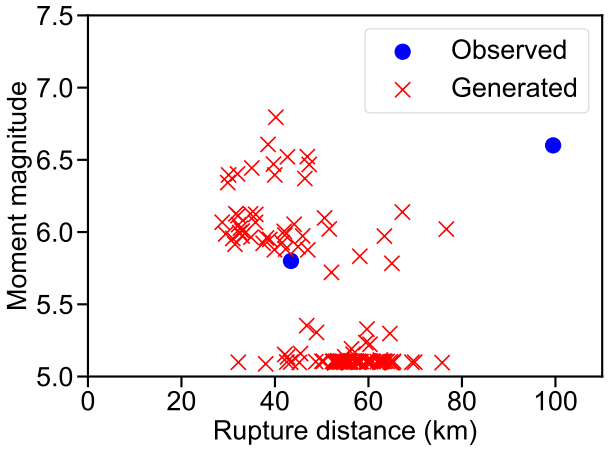

Figure 19. Magnitude-distance distribution of the observed records at YMG007 K-NET station (blue circle) and generated ground motions (red cross) with site conditions similar to YMG007 station.

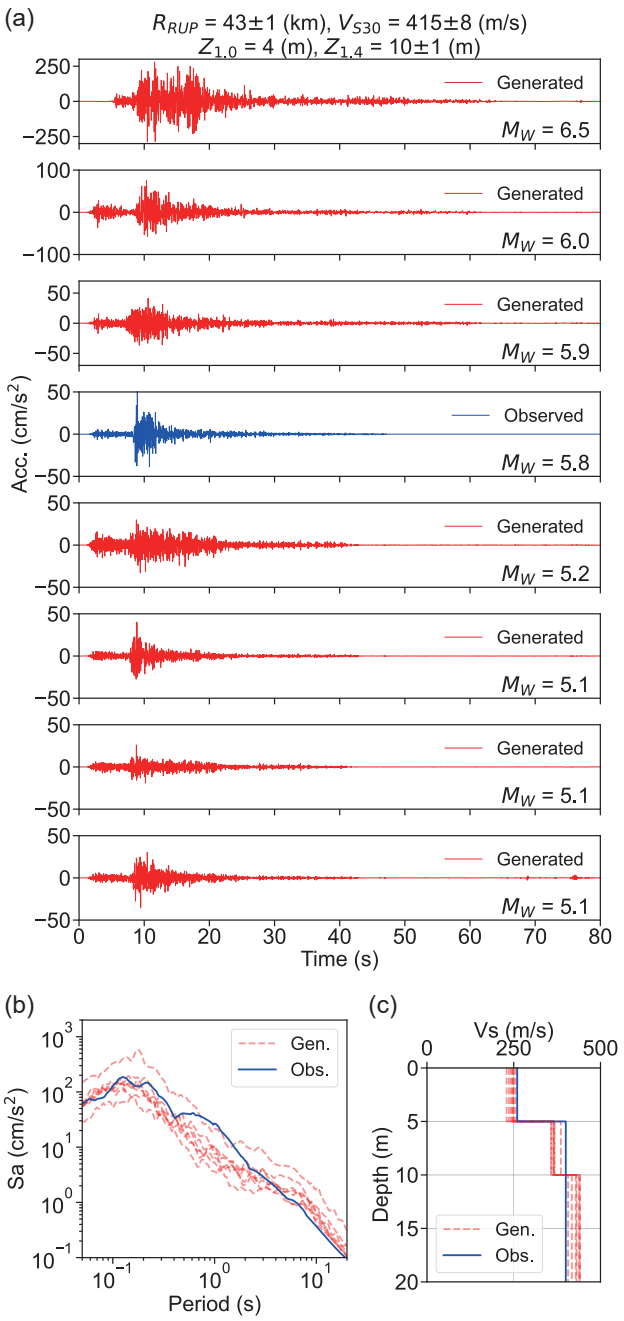

Figure 20. Ground motion waveforms (a), their corresponding acceleration spectra (b), and shear-wave velocity profiles (c) that satisfy the condition $42\,\text{km} \leq R_{RUP} \leq 44\,\text{km}$ in Figure 19. The blue solid line represents the observed record at the YMG007 K-NET station, and red dashed line represent the generated data. The shear-wave velocity profile of the YMG007 station was modeled with three layers based on the P-S logging data of the K-NET database. All condition label values for the data shown in this figure are distributed within the range indicated at the top of the figure.

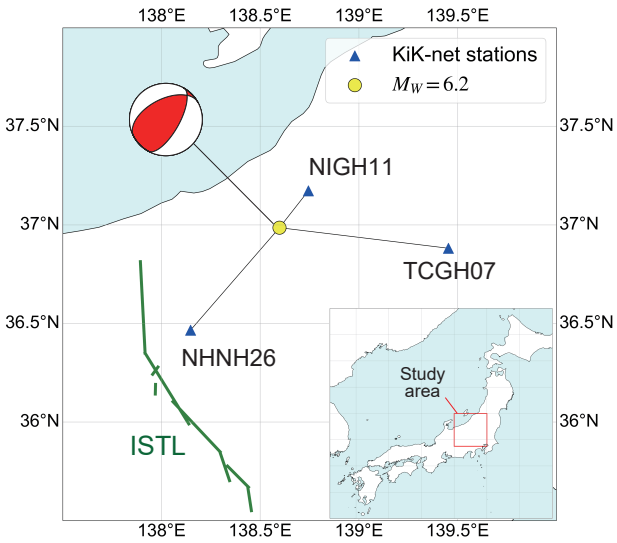

Figure 21. Locations of the epicenter of the earthquake and the target KiK-net stations TCGH07, NGNH26, and NIGH11. The focal mechanism of the earthquake was obtained from the F-net database. The green lines represent the active segments of the Itoigawa–Shizuoka Tectonic Line (ISTL) obtained from the Active Fault Database of Japan (National Institute of Advanced Industrial Science and Technology, 2024).

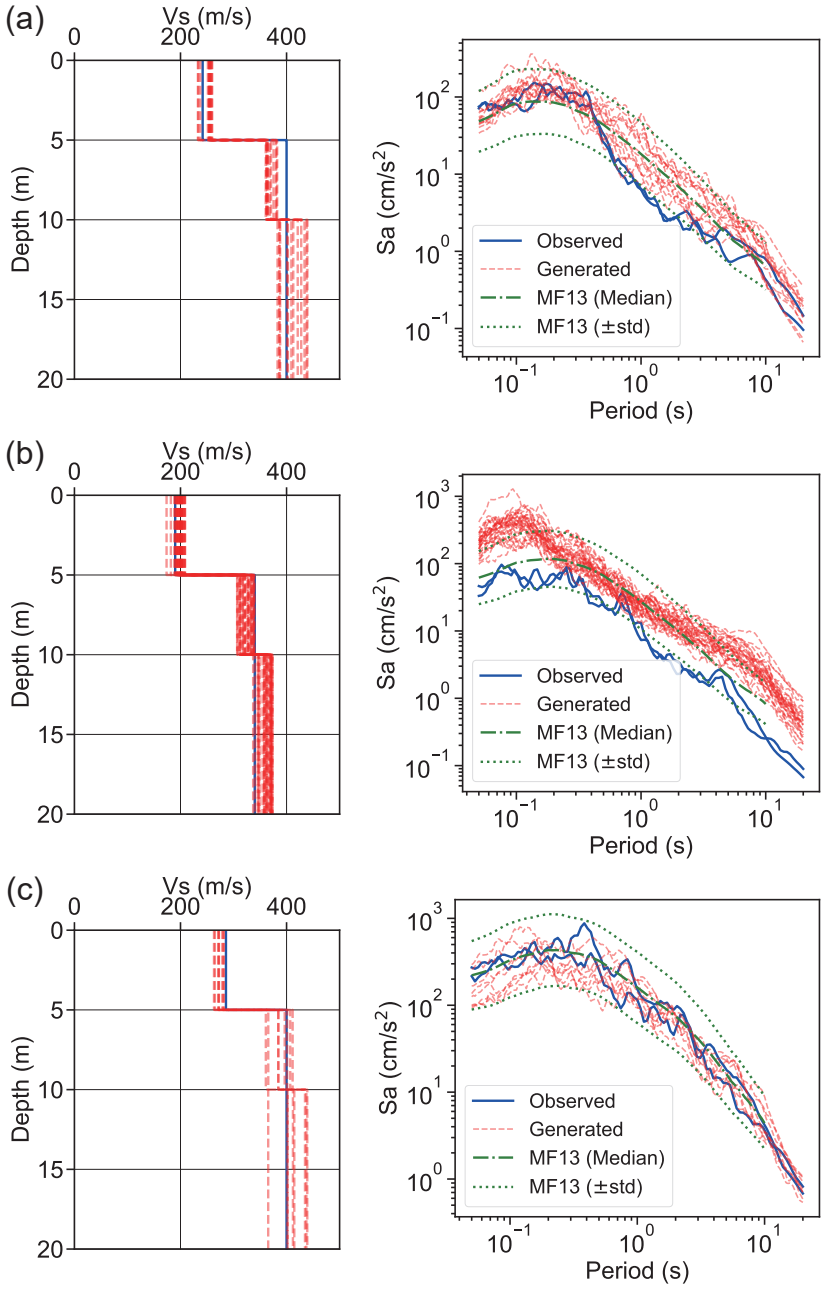

Figure 22. Comparison of shear-wave velocity profiles (left panels) and 5% damped response spectra (right panels) of the observed records versus generated ground motions for the target KiK-net stations: (a) TCGH07, (b) NGNH26, and (c) NIGH11. The blue solid lines represent the observed records, the red dashed lines represent the generated data, the green dash-dot lines represent the median of the MF13 GMM predictions, and the green dotted lines represent the ± 1 standard deviation interval of the MF13 GMM predictions.

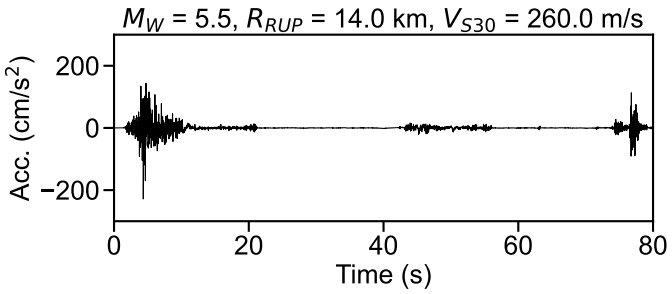

Figure 23. An example of generated ground motion waveform with subsequent oscillations showing large amplitude noise. The values at the top of this figure represent the corresponding condition label values.